

1
2
3
4
5
6
7
8
9
10
11
12
13
14
15
16
17
18

Revision 1

**Organic matter and formation of buddingtonite - an example of organic-igneous
interaction from the Paleoproterozoic Volyn pegmatite, Ukraine**

Gerhard Franz¹, Vladimir Khomenko², Aleksei Vishnyevskyy², Richard Wirth³, Ulrich
Struck⁴, Jörg Nissen⁵, Ulrich Gernert⁵, Alexander Rocholl³

¹Fachgebiet Mineralogie-Petrologie, Technische Universität Berlin, Ackerstr. 76, D-13355
Berlin, FR Germany; corresponding author gerhard.franz@tu-berlin.de

²The National Academy of Sciences, Semenenko Institute of Geochemistry, Mineralogy and
Ore Formation, 34, Palladina av., Kyiv-142, 03680 Ukraine

³Helmholtz Centre Potsdam – GFZ German Research Centre for Geosciences, Sektion 3.1,
Telegrafenberg, D-14473 Potsdam, FR Germany

⁴Museum für Naturkunde, Leibniz-Institut für Evolutions- und Biodiversitätsforschung,
Invalidenstraße 43, Berlin, D-10115, FR Germany

⁵ZE Elektronenmikroskopie, Technische Universität Berlin, Straße des 17. Juni 135, D-10623
Berlin, FR Germany

19

20 Abstract

21 The Volyn pegmatites from Volodarsk-Volynskiyi in the Zhytomyr Oblast, NW Ukraine,
22 are associated with granites genetically related to the Paleoproterozoic Korosten pluton. Their
23 late-stage evolution is characterized by the formation of opal-cemented breccia. A
24 polymineralic pseudomorph after beryl within the breccia includes bertrandite (\pm euclase) + F-
25 muscovite (with tobelite component) + buddingtonite + OM (organic matter) + opal (+ traces
26 of K-feldspar, albite, columbite, FeS₂, barite, REE-minerals). Sector zoned and platy to
27 fibrous buddingtonite has variable (K+Na)- vs. NH₄-contents (electron microprobe analyses)
28 and some H₂O or H₃O⁺, as indicated by microscope infrared spectroscopy. We suggest that
29 ammonium was produced by decay of OM, which is partly preserved in the pseudomorph.
30 Energy-dispersive electron microprobe data of the OM show with increasing O- a decreasing
31 C-N-content due to degassing; the OM contains the high-field strength elements Zr (≤ 7
32 atom%), Y (≤ 3 atom%), Sc (≤ 0.8 atom%), REE (≤ 0.3 atom%), Th (≤ 0.2 atom%) and U (≤ 1.25
33 atom%), which increase with increasing O-content. Transmission electron microscopy of the
34 OM confirms the presence of N; Zr, Si, and O (with other HFSE) are concentrated in
35 nanometer-sized areas and at the transition from OM to opal in nanometer-sized platy Zr-Si-O
36 crystals. C-rich areas are amorphous but show poorly developed lattice fringes. OM is present
37 in the pseudomorph also as brown pigmentation of opal and in pegmatitic beryl from Volyn as
38 a component in late stage fluid inclusions, identified by C-H vibrational bands in infrared
39 spectra. Stable isotope investigations of C and N of buddingtonite, black opal and kerite
40 (fibrous OM known from the literature to occur in the Volyn pegmatites and interpreted as
41 microfossils) indicate a biogenic origin of the OM. We propose that OM in the pseudomorph
42 is condensed kerite, which achieved the high concentrations of high-field strength elements
43 via fluid-pegmatite interaction. Although no age determination of minerals in the

44 pseudomorph is available, textural arguments and phase equilibria indicate its formation in a
45 late stage of the pegmatite evolution, at *P-T*-conditions below ~100 MPa/150°C. We favor a
46 conceptual model for the formation of the Volyn buddingtonite in analogy to Phanerozoic
47 occurrences of buddingtonite, where over and around the shallow anorthosite-granite Korosten
48 pluton hydrothermal convection cells introduced N-bearing hydrocarbons and its precursors
49 into the cooling igneous rocks. Due to the elevated temperature, the OM disintegrated into
50 degassing volatile and non-volatile residual components analogous to petroleum maturation.
51 Organic N, released as NH₄, was then incorporated into buddingtonite.

52

53 key words: buddingtonite, tobelite, kerite, organic matter, Volodarsk-Volynskiy pegmatite

54 field

55

56

57

Introduction

58 Nitrogen is an important trace element in crustal rocks, ranging from approximately 1 to
59 1000 ppm in igneous rocks, and from ~10 ppm to 1-2 wt% in sediments, with the highest
60 values in coal and oil shales (Holloway and Dahlgren 2002; Busigny and Bebout 2013).

61 Nitrogen is an essential compound in organic material and therefore concentrated in biogenic
62 minerals such as guanine $C_5H_5N_5O$, acetamide CH_3CONH_2 or urea $CO(NH_2)_2$. Under
63 reducing conditions, NH_4^+ can form from OM (organic matter); it has an effective radius of
64 ~0.17 nm (Pöter et al. 2007) and therefore readily substitutes for K^+ in many silicates (micas,
65 feldspars, zeolites and others). Buddingtonite $NH_4[AlSi_3O_8]$ and tobelite
66 $NH_4Al_2[(OH)_2|AlSi_4O_{10}]$ are the most common and are frequently observed as a constituent in
67 authigenic K-feldspar (e.g. Harlov et al. 2001a, and references therein) and illite (e.g. Nieto
68 2005, and references therein). Ammonium in silicates is therefore a well-established first hint
69 towards decayed OM in their sources (Ramseyer et al. 1993), and Hall (1988) already
70 suggested that the ammonium content in mafic magmas is an indicator for crustal
71 contamination. In combination with the N-isotopic signature it is now a well-established tracer
72 for OM in sediments and rocks from the deep Earth (Busigny and Bebout 2013).

73 Here we describe the pegmatitic occurrence of complex buddingtonite-K-feldspar solid
74 solutions coexisting with tobelite-rich mica, opal, and OM, which contains a high content of
75 Zr and related high field strength elements (HFSE), replacing pegmatitic beryl from the late
76 Paleoproterozoic Volyn pegmatite district from Volodarsk-Volynskiy in the Zhytomyr Oblast,
77 northwestern Ukraine. We also provide morphological data (scanning electron microscopy
78 SEM) of kerite, OM from the pegmatite. Data from electron probe microanalysis (EPMA),
79 microscope infrared spectroscopy (IR), and transmission electron microscopy (TEM), with
80 additional information from powder X-ray diffraction (XRD) and ion probe analysis of Be,

81 were applied to characterize the formation of the pseudomorph. Stable isotope data for C and
82 N of buddingtonite, opal, and kerite show the biogenic origin of OM. The Volyn pegmatite
83 represents the oldest reported buddingtonite occurrence; all others are Phanerozoic.

84

85 **Geological setting and sample material**

86 The investigated sample (stored at the mineralogical museum, TU Berlin, inv.# 2017/1)
87 was taken at the mine tailings of the Volyn pegmatite deposit at Volodarsk-Volynskyi from
88 pegmatite II. The kerite sample and black opal sample for stable isotope determination are
89 from the museum collection of the National Academy of Sciences, Kyiv. The pegmatites are
90 genetically and spatially connected with rapakivi-like differentiated granites of the Korosten
91 pluton in the northwestern Ukrainian shield (Lazarenko et al. 1973; Koshil et al. 1991;
92 Ivanovich and Alekseevich 2007). The Korosten pluton intruded high-grade gneisses some
93 1800-1760 Ma ago (Verkhoglyad 1995) and crops out over more than 15,000 km². Pegmatites
94 are found only on the western margin of this pluton in a contact zone of hybridization between
95 granite and gabbroic rocks over a distance of 22 km and on a width of 300 to 1500 m. These
96 pegmatites are known as a major source of gem minerals beryl, topaz, and quartz (variety
97 morion) and are also known for OM termed "kerite" (e.g. Ginzburg et al. 1987). Until 1996 the
98 pegmatites were mined extensively for piezo quartz, which occurs in exceptionally large
99 crystals (Lyckberg 2005; Lyckberg et al. 2009).

100 The pegmatites, typically in the range of 30 x 30 m in cross-section and 40 to 45 m high,
101 contain meter-sized miarolitic cavities and are therefore referred to as 'chamber pegmatites'
102 (information given here is summarized from Kalyuzhnyi 1982; Lyckberg 2005; Ivanovich and
103 Alekseevich 2007). They belong to the category of shallow pegmatites, residual-schlieren
104 type, fully differentiated with a distinct zonation of graphic intergrowths next to the granite
105 body, followed by a quartz-feldspar zone and a quartz core, and are irregularly distributed in

106 the granites. They belong to the Nb-Y-F enriched family, the REE subclass and the miarolitic
107 topaz-beryl interior-type (nomenclature of Černý and Ercit 2005; Černý et al. 2012). The
108 chamber can reach a volume of ca. 40 m³, in extreme cases up to 250 m³. Large quartz crystals
109 of 1 to 2 m size grew from the hanging wall into the chamber. Possibly due to fluid
110 overpressure during cooling some of the chambers were destroyed. The resulting breccia
111 consists of crystal and rock fragments, cemented by opal, chalcedony and clay minerals. The
112 investigated sample is such a breccia, which contains a pseudomorph after beryl.

113 Three different types of OM were described from the Volyn pegmatite; (i) enigmatic hair-
114 like solid material named kerite (e.g. Ginzburg et al. 1987; Luk'yanova et al. 1992; Gorlenko
115 et al. 2000; Zhmur 2003), (ii) brown pigment in black opal (Gigashvili and Kalyuzhnyi 1969),
116 and (iii) methane and dark matter in late low-temperature fluid inclusions in outer zones of
117 beryl and quartz crystals (Kalyuzhnyi et al. 1971; Voznyak et al. 2012). Proshko et al. (1987)
118 had identified buddingtonite from the Volyn pegmatites with 3-4 wt% NH₄.

119

120

Methods

121 Quantitative EMPA were obtained on carbon-coated samples with a field emission electron
122 microprobe type JEOL JXA-8530F at ZELMI at TU Berlin. Common commercially available
123 standards from Astimex were used; for N we choose boron nitride. Counting times were 10 s
124 on peak and 5 s on background. Buddingtonite is very susceptible for beam damage, and
125 therefore for most spots a beam diameter of 15 µm was chosen. Element mapping was carried
126 out with dwell time 90 ms, pixel 667 x 750, step size 240 x 240 nm. Organic matter could only
127 be analyzed with the energy dispersive method (EDS; 12 kV; 10 nA; acquisition time of ≤100
128 s), because it is even more susceptible for beam damage than buddingtonite. The absolute
129 amounts of individual elements determined by EDS are uncertain, because the relative error
130 for major elements C and O is around 10 % (as estimated by comparison of analyses on OM

131 and C-free minerals), but relative trends of element pairs are considered as reliable. For C, the
132 additional effect of the carbon coating must be considered; we choose carbon coating, because
133 coating with Au would have had a strong absorption influence on N. The EDS system is
134 equipped with a silicon drift diode detector (model EX-94310FAL1Q) and an ultra-thin film
135 window, and has an effective area of 10 mm² and an energy resolution of 128 eV (for Mn
136 K α). EDS analyses were also obtained for mineral semi-characterization, especially of small
137 inclusions. SEM images were taken with a Hitachi SU8030 instrument. Kerite was coated
138 with a ~5 nm thick iridium layer.

139 Because the sum of EPMA of an originally unknown mineral (later identified as
140 buddingtonite) was significantly <100%, we applied secondary ion mass spectrometry (SIMS)
141 to identify the missing element, which could be Be. Analyses were carried out with a Cameca
142 1280-HR ion probe at GFZ Potsdam. Using bertrandite as a standard (theoretical Be-content =
143 31.64 wt%) the determined Be concentrations in buddingtonite and muscovite (assumed Si
144 concentration: 46.5 wt%) are around 20 and 85 ppm, respectively. Li- and B-counts were also
145 checked on both minerals, again indicating concentrations at the ppm-level.

146 Two TEM foils of dimensions 15 μm x 10 μm x 0.150 μm were prepared using FIB, one (#
147 4467) crossing the boundary to opal, the other at the border to a vesicle (# 4461; for details of
148 milling see Wirth 2004, 2009). They were studied in a Tecnai F20 X-Twin TEM operated at
149 200 kV with a field emission gun as electron source, equipped with a Gatan imaging filter
150 GIFTM (Tridiem), a Fishione high-angle annular dark field detector (HAADF), and an EDAX
151 X-ray analyzer with ultra-thin window. Bright field, dark field and high-resolution TEM
152 images are usually acquired as energy filtered images applying a 20 eV window to the zero
153 loss peak of the electron energy-loss spectrum. Counting time for EDS analyses (processed
154 with TIATM software) in the scanning transmission mode across a pre-selected area thus
155 avoiding mass loss during the data acquisition, was 60 to 120 s. Electron diffraction data were

156 acquired as selected area electron diffraction pattern (SAED) or derived from high-resolution
157 lattice fringe images applying a fast Fourier Transform (FFT). Electron energy loss spectra
158 (EELS; data processing with Digital Micrograph™) were acquired in diffraction mode using a
159 camera length of 700 mm. Applying a 1 mm entrance aperture the resulting acceptance semi
160 angle is 5 mrad. Dispersion was 0.1 eV/pixel, acquisition time was 1 s.

161 Single grain IR absorption spectra were measured at room temperature in the near- and
162 middle IR region in the spectral range 7000 to 1000 cm⁻¹, by means of a Bruker FTIR
163 spectrometer IFS 66 equipped with an IR-microscope. All spectra were scanned with a
164 measuring spot of 60 μm diameter, at a spectral resolution of 2 cm⁻¹. The time-averaged signal
165 was collected over 200 scans. The reference spectra were measured in air. Areas of
166 monomineralic buddingtonite with relatively large grains, homogeneous opal and OM were
167 chosen from the same thin sections where microbeam analysis was carried out. Nine pieces of
168 this buddingtonite with sufficient size for FTIR measurements were cut out from the thin
169 sections and cleaned from resin in alcohol. Where possible, the measuring area was placed
170 mainly in a large buddingtonite crystal. While these grains appear as fibrous polycrystalline
171 aggregates (however with a euhedral outline; see Results) and measuring areas exceed
172 individual fibers in the grains, spectra were measured in unpolarized light. FTIR
173 measurements of muscovite-tobelite mica, opal and organic material were carried out in
174 uncovered thin section. Reference spectra were taken in sample-free area of the thin section
175 slide with thin epoxy layer.

176 Stable isotope analysis and concentration measurements of nitrogen and carbon were
177 performed simultaneously with a THERMO/Finnigan MAT V isotope ratio mass
178 spectrometer, coupled to a THERMO Flash EA 1112 elemental analyzer via a
179 THERMO/Finnigan ConFlo IV- interface in the stable isotope laboratory of the Museum für
180 Naturkunde, Berlin. Stable isotope ratios are expressed in the conventional delta notation

181 ($\delta^{13}\text{C}$ / $\delta^{15}\text{N}$) relative to atmospheric nitrogen (Mariotti 1983) and VPDB (Vienna PeeDee
182 Belemnite standard). Standard deviation for repeated measurements of lab standard material
183 (peptone) is generally better than 0.15 per mill (‰) for both N and C. Standard deviations of
184 concentration measurements of replicates of our lab standard are <3% of the concentration
185 analyzed.

186

187

Results

188 Petrography

189 The handspecimen shows typical breccia phenomena (Fig. 1a) with clasts of albite, alkali
190 feldspar, and quartz, which are embedded in a matrix of dominantly opal and vesicles. The
191 pseudomorph after beryl is well visible with a hexagonal outline and a core-rim structure. The
192 rim (Fig. 1b) consists of opal and bertrandite, followed by a broad zone of dominantly
193 buddingtonite and muscovite, with minor amounts of bertrandite. The core consists of very
194 fine-grained brownish Fe-rich muscovite, with some Fe-staining. OM is visible as an opaque,
195 approximately 1 x 2 mm large spot within the buddingtonite rich zone. Although mostly
196 coherent, the sample had to be embedded in epoxy resin for thin section preparation.

197

198 Mineral composition and textural relations in the beryl pseudomorph

199 **Bertrandite and euclase.** Bertrandite $\text{Be}_4\text{Si}_2\text{O}_7(\text{OH},\text{F})_2$ is the volumetrically most important
200 Be-mineral in the pseudomorph and appears as up to almost 1 mm long euhedral, platy
201 crystals in a matrix of F-muscovite (Fig. 2a,c), buddingtonite and opal. It was verified by
202 powder XRD, and EDS analyses show ~2.5 wt% of F-content. Slight corrosion features are
203 visible in contact to buddingtonite and opal. Euclase $\text{Al}[\text{BeSiO}_4(\text{OH},\text{F})]$ is rare, occurs in close
204 association with buddingtonite (Fig. EA 1), and shows minor ZrO_2 and GeO_2 contents (≤ 1
205 wt%, EDS determination).

206 **Buddingtonite.** It occurs dominantly in a network of euhedral, platy appearing crystals,
207 together with F-muscovite and opal (Fig. 2c,d,e,f), and replacing K-feldspar (Fig. 2e) and
208 albite (Fig. 2g). Replacement of albite results in randomly oriented crystals, replacement of K-
209 feldspar in oriented overgrowths. Buddingtonite appears as crystals several tens of μm large
210 with typical sector zoning (Fig. 2e; for details of sector zoning see Fig. EA 2). Euhedral
211 appearing crystals consist of μm -sized fibers indicated by slightly different extinction position
212 in thin section. Solid solution of dominantly $\text{NH}_4\text{-K}$ creates a strong variation in BSE contrast.
213 There are also intermediate euhedral-fibrous textures (Fig. 2f) with clear zoning in the core,
214 extending outwards into fibrous aggregates.

215 Buddingtonite was very difficult to analyze, because (i) it is not stable under a focused
216 beam, (ii) the inherent problems of N as a light element, and (iii) the absence of appropriate
217 standards (leading probably to a slight N over-determination). It was first without
218 determination of N, to obtain an average value for all other determined elements. The average
219 value for 26 analyses for SiO_2 with 67.24 wt% has only a very limited variation of ± 0.7 wt%;
220 the same is true for Al_2O_3 with 18.95 wt% ± 0.4 wt%, with an estimated relative error of 1-2
221 % (Table 1; individual analyses in Appendix). Titanium, Mg, Mn, Ca, Cs and Rb are always
222 close to or below the detection limit (≤ 0.01 wt% oxide). Fluorine was analyzed to check for
223 overlapping analyses with muscovite and for all analyses with detectable F some overlap must
224 be considered. Iron (average 0.08 Fe_2O_3 tot) is above the detection limit and in the formula
225 calculation attributed to the T-site. In contrast to the constant Al-Si values, K_2O varies
226 significantly between ~ 2 and ~ 5 wt%. Na_2O is low, maximum 0.9, average 0.3 wt%. In a
227 second step, we analyzed especially for N and choose the average value for SiO_2 (67.24 wt%)
228 and for Al_2O_3 (18.95 wt%) for the correction procedure (Table 1). There is no correlation
229 between $(\text{NH}_4)_2\text{O}$ and the sum of the alkalis ($\text{K}_2\text{O}+\text{Na}_2\text{O}$) (Fig. 3a). The total of the
230 determined wt% including N calculated as $(\text{NH}_4)_2\text{O}$ is in many analyses significantly below

231 100 wt%, especially for analyses with low N-content (no. 3,4 and 5 in Table 1), pointing to a
232 significant amount of "water" compound (either H₂O or H₃O⁺), which has been predicted to
233 occur in buddingtonite and discussed by Barker (1964), Laricheva et al. (1993), and Harlov et
234 al. (2001a). Na₂O and K₂O are also not correlated (Fig. 3b), all analyses show random
235 scattering.

236 X-ray mapping (WDS) of the major components (Figs. 4, 5) highlights the zoning. There is
237 a good positive correlation of K with Na, which are both low in the cores of the crystal (Fig.
238 4), but sectors enriched in K do not show Na enrichment; this might be partly due to the
239 generally low Na-contents, but also due to complex substitution including "water". A lack of
240 correlation is also seen in the compilation of all analyses (Fig. 3), and we conclude that from
241 crystal to crystal and within the crystals the amount of substitution of N-K-Na in combination
242 with H₃O⁺ differs. Note that for quantitative analyses the beam diameter was 15 μm, so it
243 averages over heterogeneities within a crystal.

244 **White mica.** Muscovite occurs as a network of platy, randomly oriented crystals with
245 interstitial opal and vesicles (Fig. 2a,b). In areas rich in buddingtonite, K is often observed to
246 be partly replaced by NH₄ (visible as lower BSE-contrast) parallel to the cleavage planes and
247 outer (001) faces (Fig. 2b,d), and also when crystals are kinked. Thin plates of muscovite in a
248 matrix of buddingtonite (Fig. EA 1) are interpreted as relicts. Quantitative analyses (Table 2)
249 show up to 25 mol% tobelite-component. The interlayer occupancy varies from 1.7 to 2 atoms
250 per formula unit, with two analyses >2.0, both with high N-content, suggesting inaccurately
251 high N. In bright areas in muscovite the N-content is below detection limit. Fluorine is
252 variable, in some analyses with >50 mol% of the F-muscovite endmember. We checked for
253 Be, B and Li with SIMS, but they are only present at the ppm-level. Silicon is higher than the
254 theoretical value of 6.0, for most analyses between 6.4 and 6.8, one point with 7.3. Total Al is
255 consistently low, on the average between 4.5 and 5.5 instead of the theoretical value of 6, and

256 the sum of octahedral occupancy is always below 4.0. Powder XRD pattern shows in addition
257 to the muscovite peaks, a broad elevated background area between 19 and 24 °2 θ typical for
258 opal, and several peaks typical for tridymite. IR characteristics (see below) also confirm that it
259 is muscovite-type mica. X-ray mapping confirms the replacement of K by N (Fig. 5); F is
260 concentrated mostly in the inner parts of the crystals (Fig. 4).

261 **Opal.** It is a volumetrically important phase (Figs. 6a, 2a) filling interstices between
262 buddingtonite (Fig. 2d). Euhedral buddingtonite crystals within opal (Fig. 2a) indicate
263 precipitation of opal slightly later or coeval with buddingtonite. Opal is strongly zoned in BSE
264 images, outer rims with lower average atomic number point to higher water contents. Internal
265 structures show concentric zoning and botryoidal growth. Opal is rich in nm to μ m sized
266 inclusions (Fig. 6b); EDS analysis show FeS₂, BaSO₄ and a phosphate-silicate phase, rich in
267 Th and Ca with minor amounts of La, Ce, Y and U (possibly brittolite-apatite).

268 **Other minerals.** K-feldspar (Fig. 2e), albite (Fig. 2a), columbite-Fe and bastnäsité-Ce are
269 interpreted as relict minerals from the pegmatitic (transitional to hydrothermal) stage because
270 of their typical corrosion features. Columbite (Fig. EA 3) and bastnäsité (Fig. EA 4) were
271 identified by EDS. Bastnäsité is replaced by opal and an unidentified LREE-phosphate with
272 botryoidal shape. Other secondary LREE-minerals were observed along dissolution features in
273 albite (Fig. 2h) and also as overgrowths on the rims of muscovite.

274 **Organic matter.** It was found in one spot in the pseudomorph (Fig. 6c-f; see also Fig. 1),
275 closely associated with opal. BSE images show a conspicuous pattern with variable
276 brightness. Brighter areas have a high content of O together with Zr, Si, Y, Sc, U, Th, with
277 minor amounts of REE and other elements, and dark areas are high in C (Table 3; Fig. 7). This
278 points to variable degrees of degassing of the OM. Along voids and vesicles, brightness is
279 very high towards the rim (Fig. 6b). Voids (Fig. 6c) and round vesicles of 1-2 μ m in size (Fig.

280 6d-f) are interpreted as degassing structures of OM. Shrinking cracks in OM are partly filled
281 by opal, indicating the presence of the OM before precipitation of opal.

282 Carbon and O are negatively correlated, from <15 atom% O to up to 40 atom% O (Fig. 7a).
283 Zirconium, which is considered as a non-organic derived HFSE, and Si (not shown) are
284 positively correlated with O (Fig. 7b), whereas N is positively coupled with C and thus also an
285 element lost from OM during degassing (Fig. 7c). Phosphorous and F are concentrated during
286 degassing (Fig. 7d). Sulfur is negatively correlated with C, from ~0.1 to 0.3 atom% at high C-
287 contents, but at lower C-contents it scatters at a rather small range of 0.35 to 0.45 atom% (Fig.
288 7h). Individual HFSE show a good positive correlation, e.g. between Sc and Y (Fig. 7f), Th
289 and U (Fig. 7g), and Y and the sum of REE (Fig. 7h).

290

291 **IR data**

292 We observed two types of unpolarized IR spectra of buddingtonite aggregates; the first one
293 represents the “pure” etalon spectrum of the tetrahedral ammonium molecule, whereas spectra
294 of the second type represent a combination of NH_4^+ and H_2O (or H_3O^+) vibrations (Fig. 8a).
295 The spectra of water-free buddingtonite are dominated by bands of the asymmetric bending
296 mode ν_4 at 1430 cm^{-1} and both symmetric ν_1 and asymmetric ν_3 stretching vibrations at 3050
297 and 3268 cm^{-1} . The latter two form envelopes together with a first overtone of ν_4 at 2846 cm^{-1} .
298 Weak bands are also clearly resolved at 1680 and 4715 cm^{-1} . In comparison to synthetic
299 buddingtonite we assigned them to symmetric bending ν_2 and a combination of $\nu_3 + \nu_4$
300 vibrations, respectively (Table 4).

301 Unpolarized IR-spectra of ammonia-bearing muscovite, measured in uncovered thin
302 section, show in addition to weak NH_4 bands those of OH at 3330 cm^{-1} and OM at $2950\text{-}2870$
303 cm^{-1} (Fig. 8). For comparison spectra taken in basal sections of single crystals of natural NH_4 -
304 bearing muscovite (California) and pure muscovite (Polar Ural; both from own collection) are

305 shown (for band assignment, see Table 4). In IR spectra of brown opal (Fig. 8c), measured in
306 uncovered thin section and in a free thin slab of opal on the border of buddingtonite
307 aggregates, the area of C-H vibration is superimposed by a broad, H₂O-dominant stretching
308 vibrations' envelope ($\nu_1 + \nu_3$) at ca. 3400 cm⁻¹ and a weak H₂O combination band ($\nu_2 + \nu_3$) at
309 5200 cm⁻¹. The IR spectra of OM was measured in uncovered thin section and shows
310 characteristic bands for C-H vibrations between ~2800 and 3000 cm⁻¹, together with broad
311 absorption in the range from 3000 to 3650 cm⁻¹ caused by O-H bonds (Fig. 8d).

312

313 TEM

314 Two FIB-foils were cut, one over the boundary from OM to opal, the other one in OM with
315 a vesicle. The foil over the boundary from OM to opal (Fig. 9a) shows an approximately 500
316 nm wide area, where platy crystals of Zr-silicate are concentrated near to the OM. In the
317 HAADF image opal shows ~5 nm large bright areas (Fig. 9b), where besides Si and O small
318 amounts of Ba, Fe, C, S, Cl, and K could be detected (spectra in Figs. EA 5, 6). The presence
319 of C confirms the IR-data about OM incorporated into opal. In the Zr-silicate also small
320 amounts of Y, U, Ca, Sc and Fe were detected by EDX. Opal and the OM are essentially
321 amorphous but with ~5 nm areas with a slight indication of lattice fringes (Fig. 9c,d).

322 The HAADF image (Z-contrast) of the FIB-foil cut over the boundary from the OM to a
323 vesicle (Fig. 10a) shows an approximately 50 nm wide rim towards the vesicle with high
324 contrast (Fig. 10b), where Zr, O, and Si are enriched together with some Al, Ca, Th, U, and Y;
325 darker areas have a higher C and lower O content. A 150 nm wide scanned EDX profile (Fig.
326 10e) in the rim shows parallel enrichment of Zr, O, and Si, and independent variation of C.
327 EELS mappings of C and O show an irregular distribution of ~10 to 30 nm wide areas, where
328 high C-contents are correlated with low O-contents and vice versa. EELS analysis in both
329 FIB-foils confirm the presence of N with a N-K edge at 400 eV.

330

331 **Kerite characterization and C-N stable isotopes**

332 Kerite is brownish-black and SEM images show typically branched fibers several 100 μm
333 in length and approximately 3 μm thickness, with a very smooth surface (Fig. 11), but with no
334 indications for segmentation. Fibers are brittle and broken cross sections show a hollow core
335 of variable diameter, but typically in the range of 250 nm x 500 nm. Unbroken fibers end in a
336 smooth round tip. The only clear indications for diagenetic alteration are mineral grains
337 (feldspar, mica, clay minerals) on the surface.

338 Stable isotope determination of buddingtonite concentrate (+ opal, white mica) from the
339 pseudomorph and from black opal yielded positive $\delta^{15}\text{N}$ (vs air) values between 1.0 ‰ and
340 2.9 ‰ (± 0.15 ‰); negative $\delta^{13}\text{C}$ (VPDB) values between -25.7 ‰ and -26.9 ‰ (± 0.15
341 ‰; Table ; Fig. 12). Kerite has a slightly higher $\delta^{15}\text{N}$ of 2.9 - 3.5 ‰ and an extremely low
342 value of -40.6 ‰ for $\delta^{13}\text{C}$.

343

Discussion

344 ***P-T-X-conditions***

345 The formation of buddingtonite in the Volyn pegmatite requires strong interaction of
346 biogenic material with the igneous rocks. To discuss this process, it is first necessary to
347 estimate the physicochemical conditions *P-T-X* of the pseudomorph formation. From the
348 Volyn pegmatites, Lazarenko et al. (1967) and Bartoshinskyi et al. (1969) first described
349 bertrandite in a pseudomorph after beryl. They argued for a reaction of beryl with a K-bearing
350 fluid to form bertrandite with muscovite and silica. The K-bearing fluid that caused the reaction
351 was ascribed to the low-temperature hydrothermal period of pegmatite evolution.

352 The calculated phase diagram for beryl stability in the simplified system $\text{BeO-Al}_2\text{O}_3\text{-SiO}_2\text{-}$
353 H_2O (Barton and Young 2002) combined with our observations provide a more quantitative
354 background, keeping in mind that HF and CO_2 contents and especially NH_4^+ contents in the

355 fluid may alter the phase relations significantly. The SIMS data show, however, that
 356 bertrandite and euclase are the only minerals, which incorporate Be on the wt% level.
 357 Muscovite textures in the pseudomorph clearly indicate that it is not a primary pegmatitic
 358 mica and its Be-, Li- and B contents are on the ppm-level and can be neglected. Therefore the
 359 relevant breakdown reaction for beryl is its lower stability limit in a hydrous fluid (Fig. 13):



361 beryl K-feldspar fluid phenakite muscovite



363 quartz

364 At $P_{\text{fluid}} \leq 100$ MPa and $T \leq 250$ °C as estimated from Barton and Young (2002), reaction (1)

365 crosses the stability of phenakite:



367 phenakite fluid bertrandite

368 and continues to lower temperature with the formation of bertrandite:

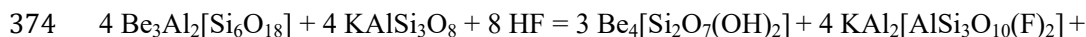


370 beryl K-feldspar fluid bertrandite

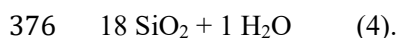


372 muscovite quartz

373 For the F-muscovite endmember the reaction is:



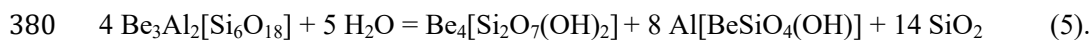
375 beryl K-feldspar fluid bertrandite F-muscovite



377 quartz fluid

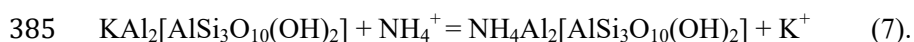
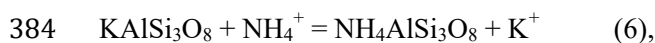
378 Where beryl is not in contact with K-feldspar, it decomposes into bertandite + euclase (Fig.

379 13), as indicated by the rare presence of euclase in the pseudomorph (Fig. EA 1):

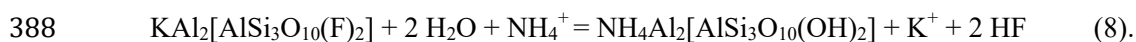


381 beryl fluid bertrandite euclase quartz

382 In the presence of an NH_4^+ -bearing fluid, K-feldspar and muscovite can equilibrate according
383 to the exchange reactions (inset in Fig. 13), forming buddingtonite and tobelite:



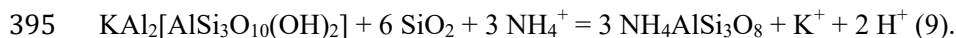
386 For F-muscovite, reaction (7) is modified to (8), keeping in mind that the newly formed
387 tobelite has less F:



389 F-muscovite fluid tobelite fluid

390 These reactions imply a scenario where first the pseudomorph with muscovite and bertrandite
391 was formed; then muscovite and relict feldspar were transformed into buddingtonite and
392 tobelite via exchange reactions with an NH_4 -bearing fluid.

393 However, muscovite can also be transformed into buddingtonite, as suggested by muscovite
394 relicts in buddingtonite (Fig. EA 1):



396 muscovite silica fluid buddingtonite fluid

397 For F-muscovite, the reaction into buddingtonite is:



399 F-muscovite silica fluid buddingtonite fluid

400 Generally, in a silica-saturated environment with abundant quartz and opal the stability
401 fields of K-feldspar, albite and muscovite are controlled by the K^+/H^+ ratio and Na^+/H^+ ratio in
402 a fluid (Hemley and Jones 1964; Wintsch 1975). Buddingtonite with NH_4 -K-Na- H_3O solid
403 solutions and NH_4 -K-F-bearing muscovite indicate a complex composition of the fluid.
404 Furthermore, the presence of carbonate (bastnäsite, see Fig. EA 4) and of CO_2 -rich fluid

405 inclusions (Kalyuzhnyi et al. 1971) requires a certain amount of CO₂ in these fluids.

406 Proshko et al. (1987) determined buddingtonite from different points in a topaz-bearing
407 chamber pegmatite from Volyn. Their observations show that buddingtonite formation via
408 exchange of alkalis by NH₄ was not restricted to the breccia and the pseudomorph: Feldspathic
409 rocks with buddingtonite formed under a zone of blocky pegmatite by leaching and
410 recrystallization, substituting the high-T assemblage quartz, feldspar and mica by the low-
411 temperature assemblage buddingtonite, albite, and hydromica.

412 Lazarenko et al. (1967) determined homogenization temperatures of liquid primary
413 inclusions (L = 85-90 vol%) in bertrandite from a pseudomorph and estimated an approximate
414 temperature of the fluid of 150 °C. The chemical composition of these late fluids is
415 characterized by high K concentration and high pH values (Kalyuznyi and Prytula 1967;
416 Kalyuzhnyi 1982). This is contradicting Černý 's (1968, 2002) compilations that bertrandite
417 forms in an acidic environment. A high pH is, however, indicated by the presence of
418 ammonia. The phase assemblages of the Be-minerals indicate a maximum temperature below
419 ~250 °C. Depending on the slope of reactions (3) and (5) at low pressure, the actual
420 temperature was probably ≤150 °C (Fig. 13).

421 Pressure conditions are difficult to estimate. The geological framework implies an
422 overburden, that is thick enough to create a significant lithostatic pressure for the formation of
423 a pegmatite. The overburden must be able to seal the rock around the large chambers with a
424 volume of tens or more m³. General estimates for the crystallization conditions of miarolitic
425 pegmatites are between 200 and 50 MPa (at ~700 to 450 °C; London 2008; for a general
426 discussion of chamber formation see also London 2013). The phase equilibria of the pure Be-
427 minerals indicate a minimum pressure of ~100 MPa at 250°C (Fig. 13), which would be much
428 lower at the assumed temperature of 150 °C.

429 Formation of the breccia might have occurred during cooling when the supercritical,
430 dominantly hydrous pegmatitic fluid in the pegmatite chamber, with a significant amount of
431 HF and saturated with Si, alkalis etc., became subcritical and separated into gas and a hydrous
432 liquid. The gas overpressure led to escape of the gas and collapse of the chamber, and the
433 large amount of Si in the liquid precipitated as opal cement of the breccia. In addition,
434 significant pressure gradients are caused in the cooling igneous body itself due to the melt-
435 crystal transition and by heating pore water in a contact aureole (e.g. Svensen et al. 2010, and
436 references therein) leading to fracturing and mobilization of material from the country rocks
437 into the igneous rock.

438 **Origin of organic matter**

439 Organic or organic-derived matter occurs as NH_4 in feldspar and mica, as C-H compounds
440 in fluid inclusions in beryl and as pigmentation of opal, as condensed OM with a high content
441 of HFSE in the pseudomorph, and as kerite. Kerite is considered as the original form. It occurs
442 within the chambers, irregularly distributed, in accumulations up to 3 kg (e.g. Ginzburg et al.
443 1987; Zhmur 2003). The fibers have a diameter of $\sim 3 \mu\text{m}$ and are several 100 μm long, similar
444 to what has been described as "monkey hair" in brown coal of Germany (reference Orlov and
445 Uspenskii 1936, in Zhmur 2003). The Volyn kerite consists of amorphous graphite-type
446 material with low structural arrangement and non-graphitized naphthenic substance (Zhmur
447 2003). Gorlenko et al. (2000) determined it as original biomass of cyanobacteria, although an
448 abiotic origin was also discussed (see references in Zhmur 2003, and Gorlenko et al. 2000).
449 The stable isotope data (Table 5) with the extremely low value of -40.6‰ for $\delta^{13}\text{C}$ clearly
450 points to its biotic origin. Furthermore, the data are consistent with anoxic methanogenic
451 bacteria (Fig. 12), typical organisms of the deep biosphere. The heavier composition of $\delta^{13}\text{C}$
452 in the buddingtonite concentrate (with opal) and of black opal itself is consistent with

453 degassing of kerite into the observed OM in the pseudomorph, where C was likely mobilized
454 as CH₄ and NH₄.

455 When the breccia with the assemblage betrandite ± euclase + muscovite formed, the OM
456 produced NH₄ to convert muscovite into the tobelite component and relict K-feldspar and
457 albite into buddingtonite. Mäder et al. (1996) showed the relevant reactions in a schematic log
458 activity (NH₄⁺/H⁺)-(K⁺/H⁺)-diagram (their Fig. 3; at 298.15 K/1 bar). However, due to the
459 enlarged stability field of F-muscovite compared to pure muscovite, the topology of the
460 system is slightly changed allowing for reaction (10), the transformation of F-muscovite into
461 buddingtonite (inset in Fig. 13). With increasing (NH₄⁺/H⁺), F-muscovite reacts into tobelite
462 (reaction 8) and then with further increasing (NH₄⁺/H⁺) into buddingtonite (reaction 6).
463 Kaolinite (not observed in our sample, but described by Lazarenko et al. 1967, from a
464 pseudomorph) is probably a later product of K-feldspar and/or muscovite alteration.

465 The OM in the pseudomorph is similar to kerite, but not in the typical fibrous form. We
466 postulate that it was first incorporated into the pegmatite chamber as kerite, and then during
467 fluid-rock interaction with fluids of the pegmatite, the kerite fibers condensed into the now
468 observed aggregate. The liberated NH₄ converted feldspar and mica into buddingtonite and
469 tobelite. The dominantly amorphous character of the OM is consistent with a low temperature.
470 Kerite composition (as given by Ginzburg et al. 1987; C 60-70 wt%; H 5-7 wt%; O 9-23 wt%;
471 N 8-9 wt%; S 2-3 wt%) in terms of C-O-N fits the general trend, which we observe, with the
472 low O-, high C-contents (Fig. 7a; recalculated into atom%). Nitrogen is high, but fits to the
473 trend of strongly decreasing N-contents down to a level of ~2 atom% (Fig. 7c).

474 With increasing condensation the amounts of HFSE increase (Fig. 7), best visible by the
475 conspicuous BSE contrast pattern (Fig. 6). The OM was enriched via interaction of the
476 hydrothermal fluids with the granitic-pegmatitic rocks, leaching HFSE, Si and other elements
477 from the pegmatite minerals (such as bastnäsite observed as a relict in the pseudomorph; Fig.

478 EA 4). Mobility of the light REE is indicated by precipitation of LREE-minerals long grain
479 boundaries (Fig. 2h). At the margin of the OM, the enrichment was large enough to precipitate
480 nanometer-sized crystals of an unidentified Zr-silicate (Figs. 9, 10). The OM itself did not
481 convert into graphite, as indicated by the only poorly developed lattice fringes (Fig. 10), and
482 consistent with the low temperature at this stage. Schilling et al. (2015) reported Zr-F transport
483 in a Be-mineralization in granite from Norway, causing precipitation of zircon in beryl-
484 phenakite reactions. In the Volyn pegmatite, mobilization of Zr, REE, Y, Sc, U, and Th and
485 trapping in OM (Fig. 7) via F-complexes is also a likely mechanism to concentrate these
486 elements. Gysi and William-Jones (2013) have shown that hydrothermal mobilization of Zr
487 and light REE in HCl-HF bearing fluids is likely controlled by pH, ligand formation, and
488 temperature. The abundance of topaz in the pegmatites and of F in the pseudomorph minerals
489 clearly indicates a high F activity. High Sc concentrations, such as observed in the Zr-enriched
490 OM from Volyn (Fig. 7f) are not unusual; Cook et al. (2013) observed Sc concentrations in
491 zircon in the same order of magnitude (up to 0.8 wt%) in a hydrothermal REE-deposit.

492 Opal is the latest mineral, cementing the breccia and also filling cracks in the condensed
493 OM. Some of the opal, appearing brown in thin section, clearly contains C-H compounds (Fig.
494 8). According to Gigashvili and Kalyuzhnyi (1969) black opal occurs as one of the last
495 minerals in the central pegmatite zone in voids in quartz. X-ray data indicate opal-CT. They
496 determined the composition of gases released upon heating to 340 °C from opal and found a
497 wide range of alkanes from methane to hexane, and possibly higher, with a mass ratio C:H =
498 84.7:15.3, close to natural oil. The authors speculated about deposition of OM in Volyn
499 pegmatites simultaneously (or soon after) with coagulation of the colloidal silica solution.
500 Hydrocarbons were also observed in a fluid inclusion in beryl on a healed crack in beryl,
501 where a second generation of beryl was precipitated (Voznyak et al. 2012). This points to
502 temperatures for the late stage of OM-incorporation at least in parts of the pegmatite field

503 above the thermal stability of beryl, depending on pressure near to ~150 °C (Fig. 13).
504 Kalyuzhnyi et al. (1971) also observed OM in complex primary CO₂-inclusions and in large
505 secondary inclusions in quartz, which contain thin crusts of material, insoluble in acids and
506 alkalis on the walls. This substance disappears when heated in air at 340–450°C. Mass
507 spectrometry revealed H₂, N₂, methane, ethane and other hydrocarbons of mass 80-115,
508 similar to the analysis of black opal (Gigashvili and Kalyuzhnyi 1969).

509 The processes are summarized in Figure 13. It started with the igneous (transitional to
510 hydrothermal) crystallization of beryl and K-feldspar in the chambers (stage 1). Possibly, in
511 the surrounding and overlying rocks, bacterial life (Gorlenko et al. 2000) boomed in surficial
512 ponds and/or sub-surface hydrothermal convection. Since kerite was observed in the chamber
513 (Zhmur 2003; Lyckberg et al. 2009), bacterial life was apparently also present as deep
514 biosphere; temperatures would be constrained by the thermal barrier of microbial life (stage
515 2). The chamber collapsed (stage 3) and in this realm, the pseudomorph with bertrandite ±
516 euclase + F-rich muscovite formed (stage 4). The ongoing fluid circulation produced the
517 enrichment of HFSE in the OM, which also lost its typical fibrous kerite-morphology (stage
518 5). The products of the degassing OM, CH₄ and higher C-H compounds, were incorporated
519 into fluid inclusions in beryl and quartz, and transformed muscovite into tobelite and relict
520 feldspars into buddingtonite via exchange reactions of alkalis to NH₄ (stage 6). Also,
521 buddingtonite formed as precipitates from the fluid, as indicated by the abundant irregularly
522 distributed buddingtonite crystals, which show no indication for replacement reactions.
523 Further cooling led to the precipitation of opal, which also incorporated alkanes. Finally, the
524 last hydrothermal alteration produced kaolinite (stage 7), and possibly other clay minerals,
525 reported in the literature (e.g. Lazarenko et al. 1967).

526

527

Implications

528 This study has shown that in a cooling granite-pegmatite system, OM can under appropriate
529 circumstances be incorporated into a pegmatite. The general idea regarding its origin involves
530 its incorporation into hydrothermal convection cells from ponds on the surface, where algae
531 blooms are typical, analogous to modern formation of buddingtonite or other NH₄-bearing
532 minerals in volcanic settings (e.g. Krohn et al. 1993; Bobos and Eberl 2013; Altaner et al.
533 1988). No surrounding or overlying sediments with organic matter exist, where buddingtonite
534 formation (due to contact metamorphism, comparable to the process postulated by Svensen et
535 al. 2008) has also been observed (see compilation in Mäder et al. 1996).

536 The Volyn pegmatite represents a prime example of incorporation of OM into an igneous
537 system and led to intense discussion of biotic versus abiotic origin of hydrocarbons (see
538 references in Zhmur 2003). Similar scenarios, but with igneous rocks showing less obvious
539 indications for OM, might be more common than previously thought. Due to analytical
540 problems to identify N in silicates, small amounts of NH₄ are likely overlooked.
541 Hydrocarbons, if not especially looked for, will also not be identified. Since kerite was
542 observed in the collaps breccia (Zhmur 2003; Lyckberg et al. 2009), bacterial life was
543 apparently present in the chambers; this would constrain the maximum temperatures below the
544 thermal barrier of microbial life. The Volyn pegmatites have extraordinary large chambers,
545 which might explain the strong enrichment of organic material, but smaller miarolitic cavities
546 are the rule in low-pressure granitic rocks, and in basaltic rocks small vesicles due to
547 degassing of the melt are also frequently observed. These are suitable to host the bacterial life.
548 Fibrous fossilized microbacteria were found e.g. at the Emperor Seamounts in the oceanic
549 deep biosphere (Ivarsson et al. 2008), however in much smaller quantities compared to Volyn
550 and less well preserved. Interaction of organic material with igneous systems is known also
551 from other different geological environments; Aarnes et al. (2015) have shown that in the
552 North Sea basins, volcanic intrusive sills contain a high amount of CH₄, generated in

553 sediments rich in organic carbon and incorporated into the cooling igneous rocks. Svensen et
554 al. (2008) used N content as a tracer for fluid flow in a hydrothermal vent system around sills
555 in the Karoo Basin, South Africa, and Hall (1988) has already proposed that the ammonium
556 content of mafic magmas is a good indicator for crustal contamination. CH₄ and N₂ is
557 commonly observed in gases from drill holes in Precambrian Canadian and Fennoscandian
558 shields (e.g. Sherwood Lollar et al. 1993, and references therein), interpreted as a mixing of
559 microbially biogenic and abiogenic derived fluids (e.g. Sherwood Lollar et al, 2006). It can be
560 speculated that also an ancient deep biosphere such as that from Volyn might contribute to
561 these fluids.

562 The formation of buddingtonite happened in the cooling Paleoproterozoic Korosten pluton.
563 It seems unlikely that a much younger event caused the hydrothermal alteration, because no
564 later geological activity is reported from the stable Precambrian Ukrainian shield. Weathering
565 phenomena can safely be excluded, as indicated by the large crystals of bertrandite and
566 muscovite in the pseudomorph and their textural relations; however the poor stoichiometry of
567 muscovite observed here and the characterization of these as hydromica (Proshko et al. 1987)
568 is in agreement with low temperatures. According to our literature search this is the oldest
569 reported occurrence of the ammonium minerals, and also the oldest reported occurrence of
570 amorphous opal. It belongs to the era of biomediated mineralogy (Hazen et al. 2008),
571 transitional between stages 7 of Paleoproterozoic atmospheric changes and surface oxidation
572 and stage 8 of an intermediate ocean. However, concerning the evolution of Be-minerals in
573 Earth's history, the Volyn pegmatites do not add new information, since all observed Be-
574 minerals are known from the Archean (Grew and Hazen 2014).

575 The scenario implies a terrestrial environment, and therefore already at ~1.8 Ga microbial
576 life on the continents and as deep biosphere must have been intense enough to create the
577 conditions for formation of buddingtonite and tobelite-rich mica. Kerite, an extremely well

578 preserved fossil microorganism, must have been available in very large amounts to increase
579 the activity of NH_4 to such a level that buddingtonite is stabilized (expressed as \log
580 $a(\text{NH}_4^+/\text{H}^+)$ of approximately 10; Mäder et al. 1996). Furthermore our observations show that
581 OM is able to concentrate large amounts of HFSE, which are generally considered as insoluble
582 at low temperature. This has strong implications for element mobility in diagenetically
583 overprinted organic-rich sediments.

584

585 **Acknowledgements**

586 We thank P. Nabein (GFZ) and C. Lange (TUB) for XRD work, F. Börner for some of the
587 artwork, and F. Couffignal (SIMS laboratory GFZ) for technical support. The cooperation
588 between the Ukrainian Academy of Sciences, Kyiv, and TU Berlin was generously sponsored
589 by Referat für Außenbeziehungen of TU Berlin, and a DFG-grant 463 UKR 113/96/0 to GF.
590 We thank B. Hazen and J. Boak for helpful reviews and D. London for editorial handling.

591

592 **References**

- 593 Aarnes, I., Planke, S., Trulsvik, M., and Svensen, H. (2015) Contact metamorphism and
594 thermogenic gas generation in the Vøring and Møre basins, offshore Norway, during the
595 Paleocene-Eocene thermal maximum. *Journal of the Geological Society, London*, 172, 588-
596 598.
- 597 Altaner, S. R., Fitzpatrick, J. J., Krohn, M. D., Bethke, P. M., Hayba, D. O., Goss, J. A., and
598 Brown, Z. A. (1988) Ammonium in alunites. *American Mineralogist*, 73, 145-152.
- 599 Barker, D. S. (1964) Ammonium in alkalifeldspars. *American Mineralogist*, 49, 851-858.
- 600 Barton, M. D., and Young, S. (2002) Non-pegmatitic deposits of beryllium: Mineralogy,
601 geology, phase equilibria and origin. *Reviews in Mineralogy and Geochemistry*, 50, 591-
602 691.

- 603 Bartoshinskiy, Z. V., Matkovskiy, O. I., and Srebrodolskiy, B. I. (1969) Accessory beryl from
604 chamber pegmatites of Ukraine. *Mineralogicheskiy Sbornik*, 23, N4, 382-397 (in Russian).
- 605 Bobos, I., and Eberl, D. D. (2013) Thickness distributions and evolution of growth
606 mechanisms of NH₄-illite from the fossil hydrothermal system of Harghita Băi, eastern
607 Carpathians, Romania. *Clays and Clay Minerals*, 61, 375-391.
- 608 Busigny, V., and Bebout, G. E. (2013) Nitrogen in the silicate earth: speciation and isotopic
609 behavior during mineral-fluid interactions. *Elements*, 9, 353-358.
- 610 Černý, P. (1968) Berylliumwandlungen in Pegmatiten. *Neues Jahrbuch Mineralogie*,
611 *Abhandlungen*, 108, 166-180.
- 612 Černý, P. (2002) Mineralogy of beryllium in granitic pegmatites. *Reviews in Mineralogy and*
613 *Geochemistry*, 50, 405-444.
- 614 Černý, P., and Ercit, T. S. (2005) The classification of granitic pegmatites revisited. *Canadian*
615 *Mineralogist*, 43, 2005-2026.
- 616 Černý, P., London, D., and Novak, M. (2012) Granitic pegmatites as reflections of their
617 sources. *Elements*, 8, 289-294.
- 618 Cook, N. J., Ciobanu, C. L., O'Rielly, D., Wilson, R., Das, K., and Wade, B. (2013) Mineral
619 chemistry of rare earth elements (REE) mineralization, Browns Ranges, Western Australia.
620 *Lithos*, 172-173, 192-213.
- 621 Ginzburg, A. I., Bulgakov, V. S., Vasilishin, I. S., Luk'yanova, V. T., Solntseva, L. S.,
622 Urmenova, A. M., and Uspenskaya, V. A. (1987) Kerite from pegmatites of Volyn.
623 *Doklady Akademii Nauk SSSR*, 292, 188-191(in Russian).
- 624 Gigashvili, G. M., and Kalyuzhnyi, V. A. (1969) Black opals from Volynian pegmatites,
625 containing organic matter. *Doklady Akademii Nauk SSSR*, 186, 1154-1157 (in Russian).
- 626 Gorlenko, V. M., Zhmur, S. I., Duda, V. I., Osipov, G. A., Suzina, N. E., and Dmitriev, V. V.,
627 (2000) Fine structure of fossilized bacteria in Volyn kerite. *Origin of Life and Evolution of*

- 628 the Biosphere, 30, 567–577.
- 629 Grew, E. S., and Hazen, R. M. (2014) Beryllium mineral evolution. *American Mineralogist*,
630 99, 999-1021.
- 631 Gysi, A., and William-Jones, A. E. (2013) Hydrothermal mobilization of pegmatite-hosted
632 REE and Zr at Strange Lake, Canada: A reaction path model. *Geochimica Cosmochimica*
633 *Acta*, 122, 324-352.
- 634 Hall, A. (1988) Crustal contamination of minette magmas: evidence from their ammonium
635 contents. *Neues Jahrbuch Mineralogie Monatshefte*, 1988, 137-143.
- 636 Harlov, D. E., Andrut, M., and Pöter, B. (2001a) Characterisation of buddingtonite
637 $(\text{NH}_4)[\text{AlSi}_3\text{O}_8]$ and ND_4 -buddingtonite $(\text{ND}_4)[\text{AlSi}_3\text{O}_8]$ using IR spectroscopy and
638 Rietveld refinement of XRD spectra. *Physics and Chemistry of Minerals*, 28, 188-198.
- 639 Harlov, D. E., Andrut, M., and Pöter, B. (2001b) Characterisation of tobelite
640 $(\text{NH}_4)\text{Al}_2(\text{AlSi}_3\text{O}_{10}(\text{OH})_2)$ and ND_4 -tobelite $(\text{ND}_4)_4\text{Al}_2(\text{AlSi}_3\text{O}_{10}(\text{OD})_2)$ using IR spectroscopy
641 and Rietveld refinement of XRD spectra. *Physics and Chemistry of Minerals*, 28, 268-276.
- 642 Hazen, B. M., Papineau, D., Bleeker, W., Downs, R. T., Ferry, J. M., McCoy, T. J.,
643 Sverjensky, D. A., and Yang, H. (2008) Mineral evolution. *American Mineralogist*, 93,
644 1693-1720.
- 645 Hemley, J. J., and Jones, W. R. (1964) Chemical aspects of hydrothermal alteration with
646 emphasis on hydrogen metasomatism. *Economic Geology*, 59, 538-569.
- 647 Holloway, J. M., and Dahlgren, R. A. (2002) Nitrogen in rock: Occurrences and
648 biogeochemical implications. *Global Geochemical Cycles*, 16, doi:
649 10.1029/2002GB001862.
- 650 Ivanovich P. V., and Alekseevich, D. S. (2007) Mineralogy of the Volynian chamber
651 pegmatites. *EKOST Association, Mineralogical Almanac*, 12, 128 p, Moscow.

- 652 Kalyuzhnyi, V. A., and Prytula, Z. S. (1967) Study of structural, thermodynamic and
653 geochemical conditions of camera pegmatites' deep fluids activities. In: Study of
654 geochemistry of deep fluids using carbonaceous relics and paragenetic minerals. *Geologiya*
655 *i Geohimiya Goryuchih Poleznyh Iskopaemyh*, 9, 33-54 (in Russian).
- 656 Kalyuzhnyi, V.A., Voznyak, D.K., and Gigashvili, G.M. (1971) Mineral forming fluids and
657 mineral paragenesis of chamber pegmatites of Ukraine. Kyiv: Naukova Dumka, 216 p (in
658 Ukrainian).
- 659 Kalyuzhnyi, V.A. (1982) The basis of teaching about mineral forming fluids. Kyiv:
660 Naukova Dumka, 239 p (in Ukrainian).
- 661 Koshil, I. M., Vasilishin, I. S., Pavlishin, V. I., and Panchenko, V. I. (1991) Wolodarsk-
662 Wolynskii Geologischer Aufbau und Mineralogie der Pegmatite in Wolynien, Ukraine.
663 *Lapis*, 10, 28-41.
- 664 Krohn, M. D., Kendall, C., Evans, J. R., and Fries, T. L. (1993) Relations of ammonium
665 minerals at several hydrothermal systems in the western U.S. *Journal of Volcanology and*
666 *Geothermal Research*, 56, 401-413.
- 667 Laricheva, O. O., Akhmanova, M. V., and Byvhkov, A. M. (1993) Low-temperature
668 hydrothermal synthesis of buddingtonite. *Geochemistry International*, 30, 126-132.
- 669 Lazarenko, E. K., Matkovskii, O. I., Pavlishin, V. I., and Sorokin, Ju. G. (1967) New data on
670 morphology and mineralogy of Volyn pegmatites. *Doklady AN SSSR*, 176, N1 (in
671 Russian).
- 672 Lazarenko, E. K., Pavlishin, V. I., Latysh, V. T., and Sorokin, Ju. G. (1973) Mineralogy and
673 genesis of the chamber pegmatites of Volyn. Lvov, *Vysshaja shkola*, 360 p (in Russian).
- 674 Levin, L.A., and Michener, R. (2002) Isotopic evidence of chemosynthesis-based nutrition of
675 macrobenthos: The lightness of being at Pacific methane seeps. *Limnology and*
676 *Oceanography* 47, 1336-1345.

- 677 London, D. (2008) Pegmatites. The Canadian Mineralogist, Special Publications 10, p 347;
678 Québec, Canada.
- 679 London, D. (2013) Crystal-filled cavities in granitic pegmatites. Rocks and Minerals, 88, 527-
680 534.
- 681 Lu'kyanova, V. T., Lobzova, R. V., and Popov, V. T. (1992) Filaceous kerite in pegmatites of
682 Volyn. Izvestiya Ross. Akademii Nauk Ser. Geologicheskaya, 5, 102-118 (in Russian).
- 683 Lyckberg, P. (2005) Gem beryl from Russia and Ukraine. In: Beryl and its color Varieties.
684 Lapis Intl., L.L.C., East Hampton, CT, USA, 49-57.
- 685 Lyckberg, P., Chornousenko, V., and Wilson, W.E. (2009) Famous mineral localities:
686 Volodarsk-Volynski, Zhitomir Oblast, Ukraine. The Mineralogical Record, 40, 473-506.
- 687 Mariotti, A. (1983) Atmospheric nitrogen is a reliable standard for natural ¹⁵N
688 abundance measurements. Nature, 303, 685-687.
- 689 Mäder, U. K., Ramseyer, K., Daniels, E. J., and Althaus, E. (1996) Gibbs free energy of
690 buddingtonite (NH₄AlSi₃O₈) extrapolated from experiments and comparison to natural
691 occurrences and polyhedral estimation. European Journal of Mineralogy, 8, 755-766.
- 692 Nieto, F. (2005) Characterization of coexisting NH₄- and K-micas in very low-grade
693 metapelites. American Mineralogist, 87, 205-216.
- 694 Orlov, N.A. and Uspenskii, V.A., (1936) Mineralogy of caustobioliths, Moscow: Akademiya
695 Nauk SSSR (in Russian; not seen, extracted from Zhmur 2003).
- 696 Peterson, B.J., and Fry, B. (1987) Stable isotopes in ecosystem studies. Annual Reviews of
697 Ecological Systems, 18, 293–320.
- 698 Pöter, B., Gottschalk, M., and Heinrich, W. (2007) Crystal-chemistry of synthetic K-feldspar-
699 buddingtonite and muscovite-tobelite solid solutions. American Mineralogist, 92, 151-165.

- 700 Proshko, V. Ya., Bagmut, N. N., Vasilishin, I. S., and Panchenko, V.I. (1987) Ammonium
701 feldspars from Volyn pegmatites and their radiospectroscopic properties. Mineralogical
702 Journal (Ukraine), 9, 67-71 (in Russian).
- 703 Ramseyer, K., Diamond, L. W., and Boles, J. R. (1993) Authigenic K-NH₄-feldspar in
704 sandstones: A fingerprint of the diagenesis of organic matter. Journal of Sedimentary
705 Petrology, 63, 1092-1099.
- 706 Rau, G. H., Teyssie, J. L., Tassoulzadegan, R., and Rowler, S. W. (1990) ¹³C/¹²C and, ¹⁵N/¹⁴N
707 variations among size-fractionated marine particles: implication for their origin and trophic
708 relationships. Marine Ecology Progress Series, 59, 33–38.
- 709 Rau, G. H., Riebesell, U., and Wolf-Gladrow, D. A. (1996) A model of photosynthetic ¹³C
710 fractionation by marine phytoplankton based on diffusive molecular CO₂ uptake. Marine
711 Ecology Progress Series, 133, 275–285.
- 712 Schilling, J., Bingen, B., Øyvind, S., Wenzel, T., Markl, G. (2015) Formation and evolution of
713 the Høgtuva beryllium deposit, Norway. Contributions to Mineralogy and Petrology 170:30
714 DOI 10.1007/s00410-015-1179-7.
- 715 Sherwood Lollar, B., Frapé, S. K., Fritz, P., Macko, S. A., Welhan, J. A., Blomquist, R., and
716 Lahermo, P. W. (1993)
717
718
719
720
721
- 722 Simmons, W. B. (2014) Gem-bearing pegmatites. In: Geology of gem deposits. Mineralogical
723 Association of Canada Short Course Series (L. E. Groat, ed.), 44, 257-304.

- 724 Struck, U. (2012) On the use of stable nitrogen isotopes in present an past anoxic
725 environments. In: Altenbach, A. V., Bernard, J. M. and Seckbach, J. (eds.) Anoxia,
726 evidence for eukaryote survival and paleontological strategies. Book series: Cellular origin,
727 life in extreme habitats and astrobiology, 21, 497-513, Springer, Berlin.
- 728 Svensen, H., Bebout, G., Kronz, A., Li, L., Plancke, S., Chevalier, L., and Jamtveit, B. (2008)
729 Nitrogen geochemistry as a tracer of fluid flow in a hydrothermal vent complex in the
730 Karoo Basin, South Africa. *Geochimica Cosmochimica Acta*, 72, 4929-4974.
- 731 Svensen, H., Aarnes, I., Podlachikov, Y. Y., Jettestuen, E., Harstadt, C. H., and Planke, S.
732 (2010) Sandstone dikes in dolerite sills: Evidence for high-pressure gradients and sediment
733 mobilization during solidification in magmatic sheet intrusions in sedimentary basins.
734 *Geosphere*, 6, 211-224.
- 735 Verkhoglyad, V.M. (1995) Age stages of magmatism of Korosten pluton. *Geochimiya i*
736 *Rudoobrazovanie*, 21, 34-47 (in Russian).
- 737 Voznyak, D.K., Khomenko, V. M., Franz, G., and Wiedenbeck, M. (2012) Physic-chemical
738 conditions of the late stage of Volyn pegmatite evolution: Fluid inclusions in beryl studied
739 by thermobarometry and IR-spectroscopy methods. *Mineralogical Journal (Ukraine)*, 34,
740 26-38, ISSN 0204-3548 (in Ukrainian).
- 741 Wintsch, R. P. (1975) Solid-fluid equilibria in the system $KAlSi_3O_8$ - $NaAlSi_3O_8$ - Al_2SiO_5 - SiO_2 -
742 H_2O - HCl . *Journal of Petrology*, 16, 57-79.
- 743 Wirth, R. (2004) Focused Ion Beam (FIB): a novel technology for advanced application of
744 micro-and nanoanalysis in geosciences and applied mineralogy. *European Journal*
745 *Mineralogy*, 16, 863–876. ^{[[[}SEP]]]
- 746 Wirth, R. (2009) Focused ion beam (FIB) combined with SEM and TEM: Advanced analytical
747 tools for studies of chemical composition, microstructure and crystal structure in
748 geomaterials on a nanometre scale. *Chemical Geology*, 261, 217-229.

749 Zhmur, S. I. (2003) Origin of Cambrian fibrous kerite of the Volyn region. *Lithology and*
750 *Mineral Resources*, 38, 55-73.

751

752 **Figure captions**

753

754 Figure 1. (a) Cut surface of handspecimen of breccia with the pseudomorph after beryl
755 (outlined). The matrix consists of albite (variety clevelandite), dark quartz (variety morion),
756 cemented by opal and chalcedony. (b) Thin section blocks of the pseudomorph, showing a
757 core-rim structure with a rim of opal + bertrandite (bert), a broad zone of buddingtonite (bud)
758 + muscovite (musc), with an aggregate of organic matter (C org) and a core of very fine-
759 grained muscovite with Fe-staining (musc + Fe).

760

761 Figure 2. BSE images of buddingtonite from pseudomorph. (a) Euhedral bertrandite (bert) in a
762 network of F-muscovite (musc) and with albite (alb). Rectangles indicate position of enlarged
763 parts in c, e and f, resp. (b) Muscovite partly replaced parallel to (001) and in a kink band by
764 tobelite-rich muscovite (tob). (c) Detail of (a), fibrous buddingtonite (bud) between F-
765 muscovite and opal. Rectangle indicates position of (d), enlarged part of fibrous buddingtonite
766 with opal between F-muscovite. Muscovite extending into buddingtonite (tob) shows a
767 tobelite component (lower BSE-contrast due to NH₄-replacement for K). Small white dots in
768 buddingtonite are due to beam damage with a focused beam, large circular areas traces of
769 slight damage during analysis. (e) Euhedral buddingtonite crystals in opal with typical sector
770 zoning and a relict K-feldspar (Kfsp) core. White rims on K-feldspar are enriched in Fe. (e)
771 Euhedral buddingtonite with sector zoning in opal. White dot above K-feldspar is beam
772 damage. (f) Buddingtonite in opal and muscovite. The central part shows a homogeneous low-
773 contrast area with euhedral outline and sector zoning, the outer rim is fibrous with a change in

774 low-high contrast areas. White areas with numbers 1-3 are areas of beam damage during
775 analysis. (g) Detail of (a), albite, partly replaced by buddingtonite. (h) Detail of (a), a LREE-
776 mineral with associated porosity (black) in albite.
777
778 Figure 3a,b. Chemical variation of buddingtonite, EMPA. (a) $(\text{NH}_4)_2\text{O}$ varies independently of
779 sum of $\text{K}_2\text{O}+\text{Na}_2\text{O}$, indicating the presence of H_3O^+ . (b) Na_2O vs. K_2O shows random
780 scattering of the data. Dots mark analyses with N-determination.
781
782 Figure 4. X-ray mapping and BSE image of aggregate of buddingtonite crystals (bud) with
783 characteristic sector zoning. The core zone is depleted in both, K and Na. The first inner zone
784 show two sectors enriched in K and two poor in K, but no difference in Na within these
785 sectors. The inner zone is followed by an outer zone, poor in K, and extends towards the rim
786 in fibrous crystals, indicated by a striped pattern of K-distribution. No difference in Na-
787 content is obvious in these zones. Si and Al content do not vary significantly. Al- and F-
788 mapping shows the distribution of muscovite, where F-contents are highest in central parts of
789 the crystals.
790
791 Figure 5. X-ray mapping and BSE image of buddingtonite-muscovite, together with opal. K-
792 mapping shows significant differences in different sectors and zones, N is homogeneously
793 distributed. Na-contents are low and show slightly heterogeneous distributions, however not as
794 strong as K.
795
796 Figure 6. BSE and SEM images of opal (a,b) and organic matter (c-f). Opal, replacing
797 bertrandite (bert), with botryoidal structure and a dark rim, indicating higher water content.
798 Arrow points to buddingtonite (bud) which appears as a small euhedral crystal in the center of

799 botryoidal opal. (b) Botryoidal opal, interstitial between buddingtonite. Bright dots near the
800 center of the botryoidal opal are FeS₂ and BaSO₄. (c) Overview of the aggregate of organic
801 matter (OM), within opal and muscovite (musc); rectangle indicate position of (d), which
802 shows the variable BSE contrast patterns, from dark = rich in C, to very bright = rich in
803 cations and oxygen. Arrows in (d) point to voids; around the voids the BSE contrast is higher,
804 pointing to degassing structures in the organic matter with enrichment of cations and oxygen.
805 Cracks in the organic matter (filled with epoxy, appearing black) are partly filled with opal. (e)
806 Overview of typical round structures in organic matter, next to opal. (f) SE-image from a
807 detail of round structures along a small crack, indicating that they are vesicles, interpreted as
808 degassing structures.

809

810 Figure 7 (a-h). Chemical variation of organic matter, plotted in atom% (EDS analyses).
811 Carbon content decreases with increasing brightness in BSE-images (cf. Fig. 6) linearly
812 correlated with increasing O. (b) Zr increases with O, indicating capture of Zr during
813 degassing. (c) N-content decreases with decreasing C-content, indicating loss of N during
814 degassing. (d) P is positively correlated with F, and negatively correlated with N (not shown),
815 indicating enrichment of P and F during degassing. (e) S behaves irregularly, areas rich in C
816 are poor in S, areas rich in O poor in S (see text). Y and Sc (f), Th and U (g), and Y and the
817 summ of REE are all well correlated, and also positively correlated with Zr (not shown). For
818 comparison, the average composition of kerite (asterisk), organic matter from the Volyn
819 pegmatites (Ginzburg et al 1987; Zhmur 2003; converted into atom%) is shown.

820

821 Figure 8. FTIR spectra of (a-d) buddingtonite, NH₄-rich muscovite, brown opal, and organic
822 matter from the beryl pseudomorph, Volyn. (a) Unpolarized FTIR spectra of crystal
823 aggregates of buddingtonite. Spectra are shifted vertically. Lower lines, labeled with ν_1 to ν_4 ,

824 are for buddingtonite with varying amounts of K-NH₄, upper line is for hydronium-bearing
825 buddingtonite, labeled with arrows pointing to H₃O bands, demonstrating the presence of both
826 NH₄⁻ and H₃O⁻ vibrations. The modes of NH₄ vibrations are marked according to the band's
827 assignments in Table 4. (b) Unpolarized FTIR spectra of ammonia-bearing muscovite
828 intergrowth, measured in uncovered thin section (upper, solid line), in comparison with natural
829 NH₄-bearing muscovite from California (middle, dashed line) and pure muscovite from Polar
830 Ural (bottom, dot-dash line). In Volyn sample vibration bands of H₂O at 3330 cm⁻¹ and
831 organic matter at 2950-2870 cm⁻¹ are present in addition to weak NH₄ bands. (c) FTIR spectra
832 of brown opal measured in thin section and a thin slab of opal material on the border of
833 buddingtonite grain. The area of C-H vibrations is shown as well as broad H₂O-dominant
834 stretching vibrations' band ($\nu_1+\nu_3$) at ca. 3400 cm⁻¹ and weak combination band ($\nu_2+\nu_3$) at
835 5200 cm⁻¹. (d) FTIR spectra of dark organic matter, measured in uncovered thin section.

836

837 Figure 9. TEM results foil #4667 of boundary between opal and organic matter (OM). (a)
838 Detail of HAADF (Z-contrast) image. Bright area at the rim of organic matter with platy habit
839 shows high amounts of O-Zr-Si with minor Y, U, Th, Fe, and Al contents. All EDX spectra
840 are compiled in Figs. EA 5,6. (b) Detail of HAADF image of opal with patchy contrast. Bright
841 areas show Ba, S, Fe, C, and minor K and Cl in the EDX spectra. (c) High-resolution image of
842 bright area in opal, showing the dominantly amorphous character and ~5 nm wide areas with
843 lattice fringes that indicate nanocrystalline material (arrows). (d) High-resolution image of
844 organic matter, showing patchy distribution of ~5 nm wide areas with poorly developed lattice
845 fringes.

846

847 Figure 10. TEM results foil # 4461 at the boundary of organic matter (OM) to a vesicle. (a)
848 HAADF Z-contrast image of the FIB-foil. Organic matter is essentially amorphous, showing

849 lattice fringes with spacing of ~0.33 nm in approximately 5 to 10 nm wide areas of
850 nanocrystalline material, which is enriched in O-Si-Zr (similar as in Fig. 9d). (b) Detail of rim
851 area of OM; HAADF image, upper part in (a). Rectangles indicate areas of EDX analyses with
852 higher O-Si-Zr (-Th-U-Ca)-contents in the bright areas (spectra in Fig. EA 7), line indicates
853 position of profile in (c), EDX line scan with parallel enrichment of O-Si-Zr, inversely
854 correlated with C. (d,e) EELS element mapping of O and C of OM, confirming the irregular
855 distribution of poorly crystalline material.

856

857 Figure 11. SEM images of kerite. a) overview, showing hair-like morphology; b) characteristic
858 branching, c) round end of a fiber and smooth surface; rectangular dark area is artefact due to
859 beam damage during analysis. d) Broken fiber, showing the characteristic hollow core with a
860 width of approximately 260 x 550 nm.

861

862 Figure 12. Results of organic carbon and nitrogen stable isotope determination of kerite, opal
863 and buddingtonite concentrate (with opal, tobelite). Fields for modern marine sediments,
864 phytoplankton and methanogenic bacteria are summarized from Levin and Michener (2002)
865 Peterson and Fry (1987) Rau et al. (1990, 1996) and Struck (2012).

866

867 Figure 13. Schematic *P-T* diagram, illustrating the evolution of mineral assemblages in the
868 pseudomorph after beryl (based on Barton and Young 2002); inset shows schematic fluid-
869 solid equilibria in the system $\text{SiO}_2\text{-Al}_2\text{O}_3\text{-K}_2\text{O-H}_2\text{O-NH}_3$ at quartz saturation and ambient
870 conditions, based on Mäder et al. (1996), but with an enlarged field for F-muscovite instead of
871 pure muscovite. Encircled numbers refer to reactions (see text), numbers in bold/italic to
872 formation stages. Pegmatitic crystallization started with ***1*** beryl+K-feldspar; ***2*** in hydrothermal
873 convections cell, bacterial life produced kerite in the chambers; ***3*** chamber collaps produced

874 the breccia, in which **4** the pseudomorph formed with betrandite, euclase and F-rich
875 muscovite; **5** fluid circulation enriched HFSE in kerite, and C-H fluids from degassing kerite
876 were incorporated into cracks in beryl; fluid composition was enriched in NH₄, which drove
877 the equilibrium of muscovite-Kfeldspar **6** towards the muscovite-tobelite equilibrium (reaction
878 8 in inset), and with further increase in NH₄ concentration reached reactions 10 and 6. Opal
879 precipitated as one of the last minerals; **7** late hydrothermal alteration produced kaolinite. For
880 further discussion see text.

Table 1 Buddingtonite EMPA and calculated cations per formula unit (cpfu)

wt%/no.	1	2	3	4	5	6	7	8	9	10	11	23	24	aver ^a	min	max
aver SiO ₂							67.24							67.24	66.57	67.91
TiO ₂	b.d.	0.02	b.d.	0.03	b.d.	b.d.	b.d.	0.03	b.d.	b.d.	b.d.	b.d.	0.03	0.01	b.d.	0.05
aver Al ₂ O ₃							18.95							18.95	18.68	19.41
Fe ₂ O ₃	0.09	0.23	0.11	0.13	0.05	0.03	0.10	0.06	0.05	0.18	0.04	0.66	0.46	0.08	0.01	0.19
MgO	b.d.	0.01	0.02	b.d.	b.d.	b.d.	b.d.	0.02	b.d.	b.d.	b.d.	b.d.	0.07	b.d.	b.d.	0.01
CaO	b.d.	0.04	0.05	0.07	0.07	0.01	0.01	b.d.	0.01	0.04	b.d.	0.03	b.d.	0.01	b.d.	0.04
MnO	b.d.	b.d.	0.04	0.02	b.d.	0.05	b.d.	0.01	0.05	b.d.	0.02	0.07	0.08	0.01	b.d.	0.06
Na ₂ O	0.17	0.14	0.14	0.12	0.12	0.14	0.13	0.13	0.20	0.14	0.14	0.60	0.42	0.32	0.12	0.90
K ₂ O	3.45	3.47	3.86	3.07	3.22	3.43	3.60	3.50	4.63	3.61	3.19	1.49	3.79	3.86	1.93	5.10
Cs ₂ O	0.01	0.01	0.02	b.d.	b.d.	b.d.	b.d.	0.03	0.03	0.04	0.02	0.01	0.01	0.01	b.d.	0.03
F	b.d.	b.d.	b.d.	b.d.	b.d.	b.d.	0.32	b.d.	b.d.	b.d.	b.d.	b.d.	b.d.	0.04	b.d.	0.49
(NH ₄) ₂ O	9.41	4.07	3.29	3.35	2.61	8.54	8.03	6.71	5.33	5.24	7.73	7.86	7.31	n.d.	n.d.	n.d.
	99.32	94.17	93.72	92.98	92.26	98.39	98.38	96.67	96.50	95.43	97.33	96.91	98.36	90.51	89.41	91.74
cpfu	cations per 8 oxygen															
Si	2.967	3.067	3.081	3.088	3.104	2.949	3.028	3.018	3.030	3.042	3.003	2.998	2.989			
Al	0.985	1.019	1.023	1.026	1.031	0.979	1.006	1.002	1.006	1.010	0.997	0.996	0.993			
Fe ³⁺	0.003	0.008	0.004	0.005	0.002	0.001	0.003	0.002	0.002	0.006	0.001	0.022	0.015			
Sum T	3.955	4.095	4.108	4.119	4.137	3.929	4.037	4.023	4.038	4.058	4.001	4.016	3.998			
Ca	-	0.002	0.002	0.003	0.003	-	-	-	0.001	0.002	-	0.002	-			
Na	0.015	0.012	0.012	0.010	0.011	0.012	0.011	0.011	0.017	0.012	0.012	0.052	0.036			
K	0.194	0.202	0.225	0.179	0.189	0.194	0.204	0.201	0.266	0.208	0.182	0.085	0.215			
NH ₄	0.959	0.428	0.348	0.355	0.279	0.875	0.825	0.696	0.554	0.548	0.798	0.809	0.751			
Sum	1.168	0.645	0.596	0.554	0.483	1.088	1.046	0.909	0.848	0.776	0.993	0.950	1.010			

b.d. = below detection; in cation pfu Ti, Mg, Mn, and Cs mostly below 0.001; ^a average, minimum and maximum of 26 analyses without N-determination

Table 2 Muscovite EMPA and cation per formula unit (cpfu). calculated for 24 (O. OH)

wt%/no.	V2 4	V2 6	V2 6	V2 7	V2 8	V2 9	1	2	3
SiO ₂	49.73	48.04	48.96	49.05	48.08	47.83	49.90	49.68	49.08
TiO ₂	0.01	b.d.	0.01	b.d.	0.03	b.d.	0.01	0.01	b.d.
Al ₂ O ₃	29.16	33.95	30.51	30.69	33.81	33.57	29.10	29.15	29.39
Fe ₂ O ₃	3.97	0.99	3.52	3.45	0.80	0.78	2.86	3.20	3.01
MgO	0.01	0.24	b.d.	b.d.	0.25	0.23	0.10	0.05	0.12
MnO	b.d.	b.d.	0.03	b.d.	b.d.	b.d.	b.d.	0.02	b.d.
CaO	b.d.	b.d.	b.d.	0.01	0.01	b.d.	b.d.	b.d.	b.d.
Na ₂ O	0.03	0.04	0.03	0.04	0.04	b.d.	0.04	0.01	0.04
K ₂ O	10.12	10.31	10.42	10.52	10.42	10.51	10.47	10.24	10.50
(NH ₄) ₂ O	n.d.								
Cs ₂ O	0.01	b.d.	b.d.	0.04	0.03	0.02	b.d.	b.d.	0.02
F	2.46	0.90	2.40	2.24	0.95	1.17	7.26	5.97	3.87
sum corr for F	91.23	94.03	94.69	94.90	93.94	93.53	96.11	95.34	94.10
cpfu/no.	V2 4	V2 6	V2 6	V2 7	V2 8	V2 9	1	2	3
Si	6.754	6.437	6.626	6.620	6.452	6.458	6.804	6.782	6.731
Al IV	1.246	1.563	1.374	1.380	1.548	1.542	1.196	1.218	1.269
Al tot	4.667	5.361	4.866	4.882	5.347	5.342	4.676	4.690	4.749
Al VI	3.421	3.798	3.493	3.501	3.799	3.800	3.480	3.472	3.480
Fe ³⁺	0.406	0.100	0.358	0.350	0.080	0.079	0.293	0.329	0.311
Ti	0.001	-	0.001	-	0.003	-	0.001	0.001	-
Mg	0.001	0.047	-	-	0.049	0.045	0.020	0.009	0.024
Mn	-	-	0.004	-	-	-	-	0.002	-
Sum VI	3.828	3.946	3.856	3.852	3.931	3.925	3.795	3.814	3.815
Ca	-	-	-	0.001	0.001	-	-	-	-

Na	0.007	0.010	0.009	0.010	0.011	-	0.010	0.002	0.011
K	1.754	1.762	1.799	1.810	1.784	1.811	1.820	1.783	1.837
Sum I	1.761	1.772	1.807	1.822	1.797	1.811	1.830	1.785	1.848
F	0.528	0.191	0.514	0.477	0.201	0.249	1.566	1.289	0.839

b.d. = below detection 0.01 wt%; n.d. = not determined

Table 2 cont. Muscovite

wt%/no.	14	15	16	17	18	19	20	21
SiO₂	47.51	51.33	47.66	49.66	46.85	47.63	47.86	48.14
TiO₂	0.04	0.01	0.03	0.06	0.01	0.03	b.d.	b.d.
Al₂O₃	31.39	23.41	32.58	27.66	33.19	30.12	33.09	28.03
Fe₂O₃	1.44	3.25	1.15	3.07	0.90	2.79	0.84	3.30
MgO	0.33	0.06	0.31	0.01	0.22	0.05	0.22	b.d.
MnO	0.04	b.d.	0.01	0.06	0.01	b.d.	b.d.	b.d.
CaO	0.04	b.d.	0.04	b.d.	0.01	0.03	0.01	0.02
Na₂O	0.03	0.02	0.03	0.03	0.02	0.05	0.01	0.03
K₂O	9.95	9.74	8.85	10.31	10.36	10.09	10.03	10.43
(NH₄)₂O	1.68	0.67	b.d.	b.d.	0.11	b.d.	1.23	b.d.
Cs₂O	b.d.	0.05	0.01	0.04	0.01	b.d.	0.01	b.d.
F	1.05	4.73	0.78	3.24	0.92	2.53	1.03	2.43
Sum corr for F	93.00	91.04	91.09	92.60	92.17	92.10	93.84	91.23
cpfu/no.	14	15	16	17	18	19	20	21
Si	6.489	7.294	6.535	6.895	6.422	6.621	6.446	6.778
Al IV	1.511	0.706	1.465	1.105	1.578	1.379	1.554	1.222
Al tot	5.052	3.919	5.264	4.526	5.361	4.934	5.252	4.650
Al VI	3.541	3.213	3.799	3.422	3.783	3.555	3.699	3.428
Fe³⁺	0.148	0.348	0.119	0.320	0.093	0.291	0.086	0.350
Ti	0.004	0.001	0.003	0.006	0.001	0.003	-	-
Mg	0.067	0.013	0.064	0.002	0.044	0.009	0.045	-
Mn	0.005	-	0.002	0.006	0.001	-	-	-
Sum VI	3.766	3.575	3.987	3.756	3.922	3.858	3.829	3.778

Ca	0.006	-	0.006	0.001	0.001	0.004	0.001	0.004
Na	0.008	0.006	0.009	0.008	0.004	0.012	0.003	0.009
K	1.733	1.765	1.547	1.827	1.812	1.790	1.722	1.873
(NH₄)	0.529	0.219	-	-	0.036	-	0.384	-
Sum I	2.277	1.990	1.562	1.835	1.853	1.806	2.110	1.885
F	0.227	1.063	0.170	0.711	0.198	0.556	0.219	0.540

b.d. = below detection 0.01 wt%; n.d. = not determined

Table 3 EDS analyses of organic matter (in atom%, normalized to sum = 100 %)

	PM 01	PM 02	PM 03	PM 04	PM 05	PM 06	PM 07	PM 08	PM2 01	PM2 02	PM2 03	PM2 04	PM2 05	PM2 06
C	65.01	44.00	73.70	53.46	68.87	56.50	43.35	35.83	59.98	46.01	52.02	53.51	69.95	68.8
N	n.d.	2.13	2.08	1.94	1.74	2.46	2.84							
O	27.31	37.34	21.56	32.45	24.6	30.88	37.08	40.67	27.16	36.03	30.07	30.05	20.35	21.35
F	0.58	1.3	0.001	1.19	0.44	1.01	1.20	1.63	0.93	1.19	0.90	0.80	0.41	0.49
P	0.89	2.29	0.62	1.67	0.76	1.58	2.9	3.53	1.28	2.11	1.96	1.83	0.79	0.80
S	0.33	0.37	0.24	0.41	0.32	0.38	0.39	0.22	0.32	0.34	0.37	0.39	0.27	0.30
Al	0.12	0.14	0.07	0.15	0.1	0.12	0.17	0.16	0.08	0.09	0.08	0.07	0.03	0.04
Si	1.77	4.23	1.22	3.36	1.53	2.86	4.32	5.10	2.37	3.35	3.60	3.40	1.65	1.64
Ca	0.18	0.46	0.11	0.33	0.15	0.27	0.48	0.55	0.21	0.40	0.38	0.33	0.17	0.13
Fe	0.12	0.37	0.06	0.15	0.08	0.16	0.17	0.31	0.11	0.43	0.19	0.21	0.06	0.06
Zr	2.12	5.48	1.39	3.97	1.74	3.49	5.47	6.79	3.11	4.35	4.80	4.47	2.19	2.09
Y	0.81	1.87	0.52	1.32	0.66	1.26	2.29	2.73	1.13	1.75	1.76	1.63	0.81	0.74
Sc	0.19	0.40	0.08	0.33	0.12	0.30	0.54	0.77	0.40	0.50	0.56	0.47	0.26	0.19
Ce		0.08					0.08	0.08		0.07	0.07	0.04	0.03	0.02
Pr													0.04	
Nd	0.03	0.02		0.03	0.02	0.03	0.04	0.05					0.06	
Er						0.10								
Eu									0.02					
Yb	0.07	0.16	0.07	0.15	0.08	0.14	0.19	0.23	0.12	0.20	0.16	0.15	0.09	0.09
Hf		0.08	0.03	0.05	0.03	0.02	0.05	0.07	0.07	0.15	0.12	0.09	0.06	0.07
Th	0.06	0.12	0.04	0.10	0.06	0.12	0.17	0.18	0.06	0.11	0.10	0.09	0.04	0.03

U	0.42	1.17	0.32	0.83	0.43	0.79	1.11	1.00	0.52	0.79	0.79	0.72	0.37	0.32
K														
Na										0.05				
Ba				0.06										
Ta		0.14						0.12						

n.d. = not determined; blank = not identified

Table 3 cont. EDS analyses of organic matter (in atom%)

	PM2 08	PM2 09	PM2 10	PM2 11	PM2 12	PM2 13	PM2 14	PM2 15	PM2 16	PM2 17	PM2 18
C	72.93	77.27	59.14	76.10	83.63	83.79	80.84	80.08	80.23	78.00	78.49
N	2.10	2.47	1.53	2.59	3.30	3.69	4.12	3.75	3.41	3.47	3.88
O	17.74	15.35	24.57	15.15	12.85	12.19	14.81	16.02	16.16	18.24	17.37
F	0.16	0.17	0.51	0.10							
P	0.80	0.53	1.99	0.72							
S	0.34	0.25	0.43	0.30	0.09	0.10	0.07	0.08	0.08	0.09	0.07
Al	0.06	0.08	0.13	0.07						0.07	0.05
Si	1.74	1.22	3.35	1.40	0.03	0.14	0.02	0.01	0.04	0.03	0.02
Ca	0.19	0.10	0.44	0.14	0.04	0.05	0.07	0.05	0.05	0.07	0.05
Fe	0.06	0.07	0.11	0.10							0.03
Zr	2.18	1.44	4.61	1.87							
Y	0.79	0.49	1.58	0.66							
Sc	0.12	0.10	0.31	0.10							
Ce	0.03	0.001	0.03	0.02							
Pr											
Nd											
Er											
Eu											
Yb	0.10	0.05	0.12	0.06							
Hf	0.07	0.04	0.07	0.04							
Th	0.05	0.03	0.11	0.05							

U	0.52	0.35	0.97	0.51								
K					0.01	0.01	0.01		0.01	0.01	0.01	
Na					0.04	0.04	0.06	0.02	0.03	0.02	0.03	
Ba												
Ta												

n.d. = not determined; blank = not identified

Table 4: Assignments of NH₄ vibrational bands in IR spectra of natural buddingtonite and muscovites and their synthetic analogs.

Mineral	Position of bands' maxima (cm ⁻¹) and assignments						
	V ₄	V ₂	2V ₄	V ₁	2V ₂ (?)	V ₃	V ₃ +V ₄
Buddingtonite (Volyn)	1430	1680	2846	3050	3185	3268	4715
Muscovite (Volyn)	no data	no data	2820	3044	3135	3292	not obs.
Muscovite (California)	1432	1670	2825	3034	3144	3292	not obs.
Buddingtonite synthetic ^a	1445	1690	2844	3065(V ₂ +V ₄)	3187	3288	no data
Tobelite synthetic ^b	1430	not obs.	2825	3035(V ₂ +V ₄)	3175	3300	no data

^a Harlov et al. 2001a, ^b Harlov et al. 2001b

Table 5 Results of stable isotope of N (relative to air) and C (relative to VPDB) measurements of material from Volyn pegmatite; error for both δ values is 0.15 ‰

sample	kerite	kerite	kerite	opal	opal	buddingtonite	buddingtonite
weight [mg]	1.280	1.795	2.291	41.114	40.371	50.749	41.959
$\delta^{15}\text{N}$ [‰]	3.487	3.331	2.920	0.968	2.870	1.507	2.269
mg N	0.102	0.139	0.147	0.015	0.014	0.027	0.033
wt% N	7.978	7.753	6.416	0.037	0.034	0.053	0.079
$\delta^{13}\text{C}$ [‰]	-40.630	-40.574	-40.615	-25.885	-25.656	-26.796	-26.862
mg C	0.816	1.177	1.275	0.236	0.230	0.139	0.109
wt% C	63.723	65.563	55.651	0.574	0.570	0.274	0.260

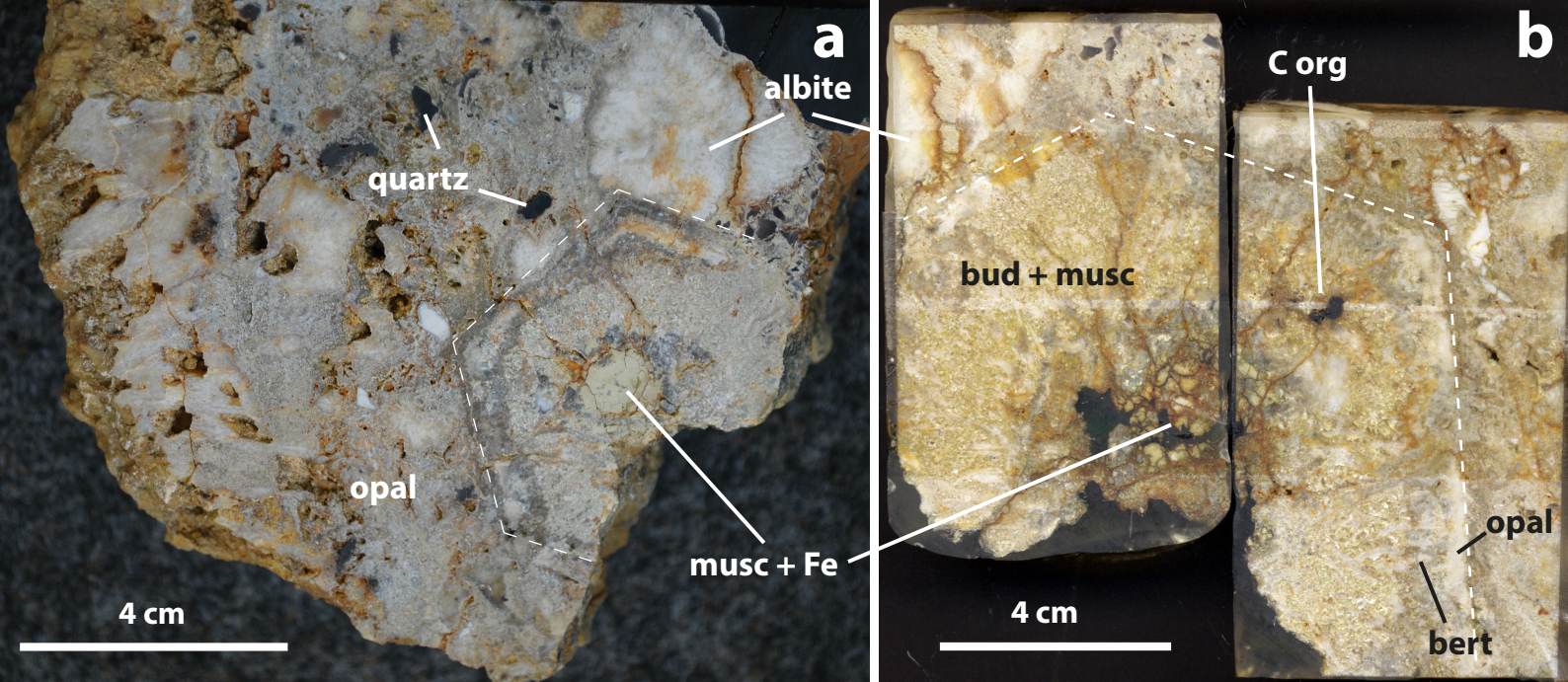


Fig. 1

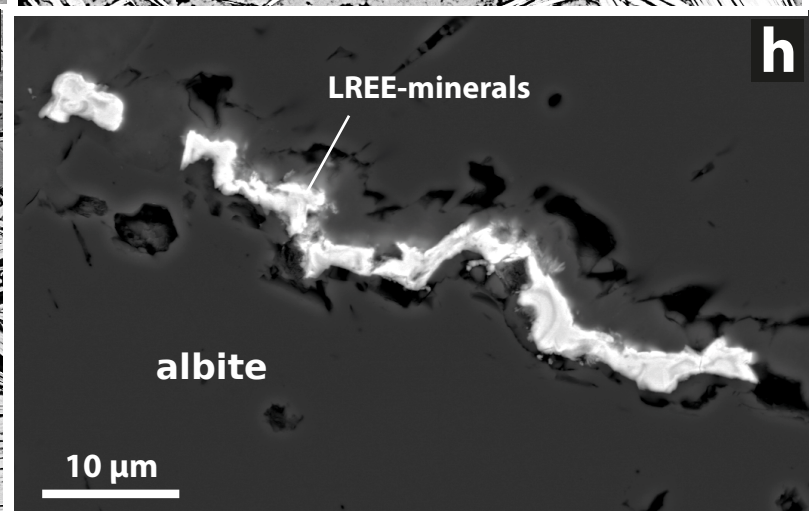
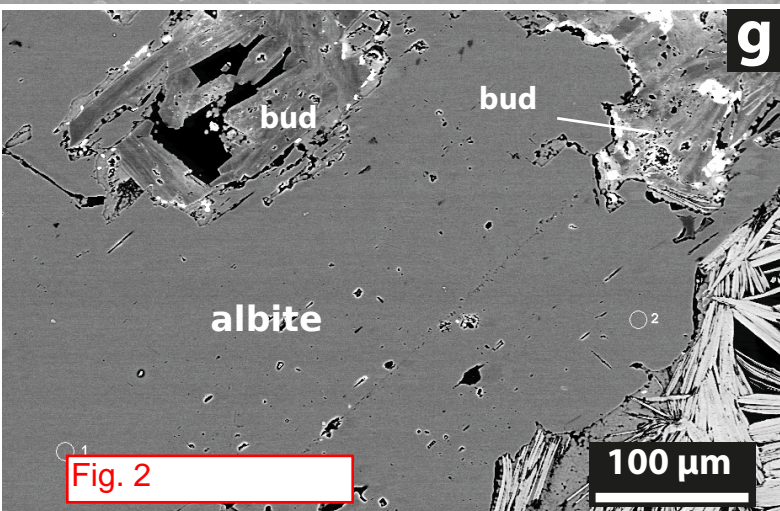
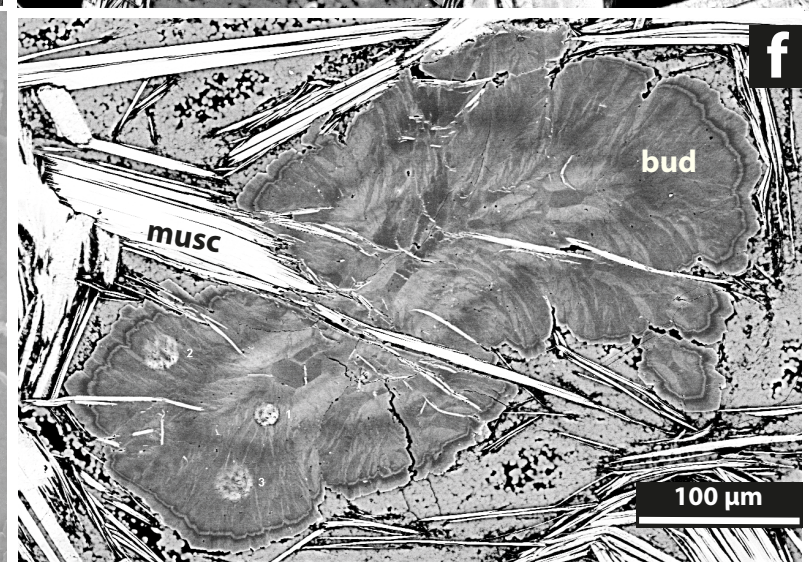
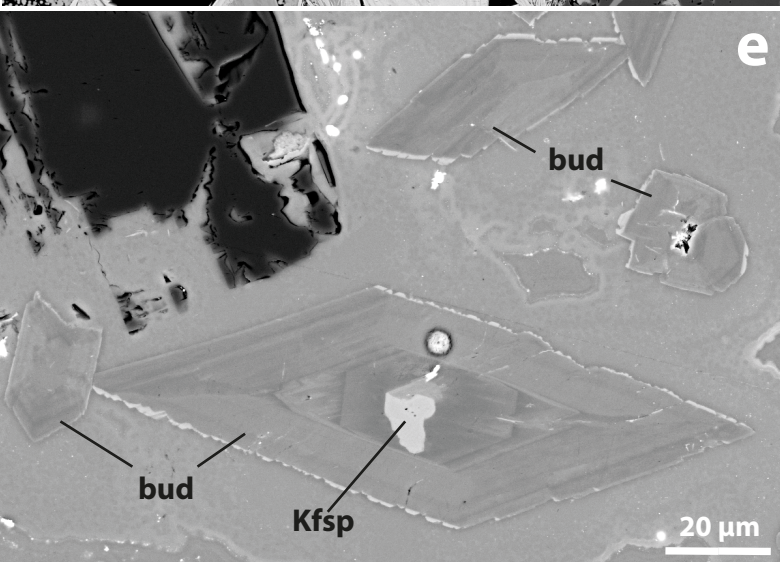
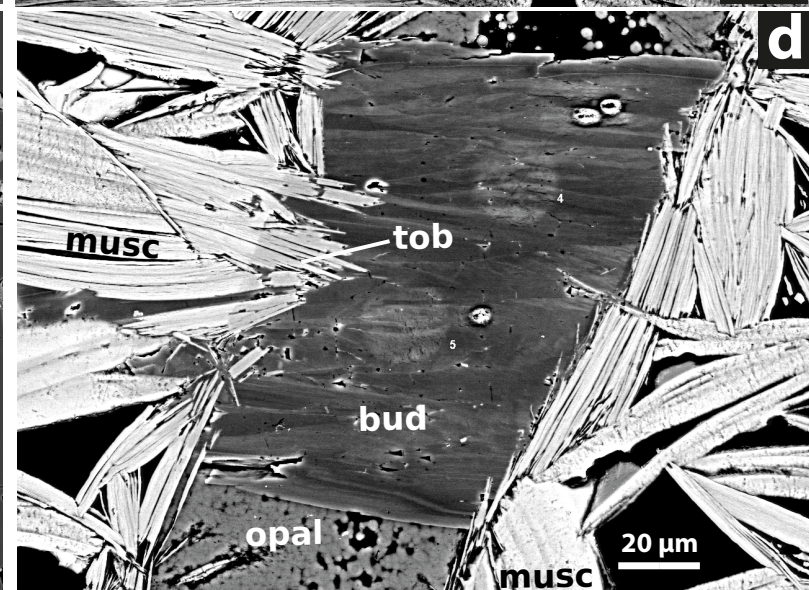
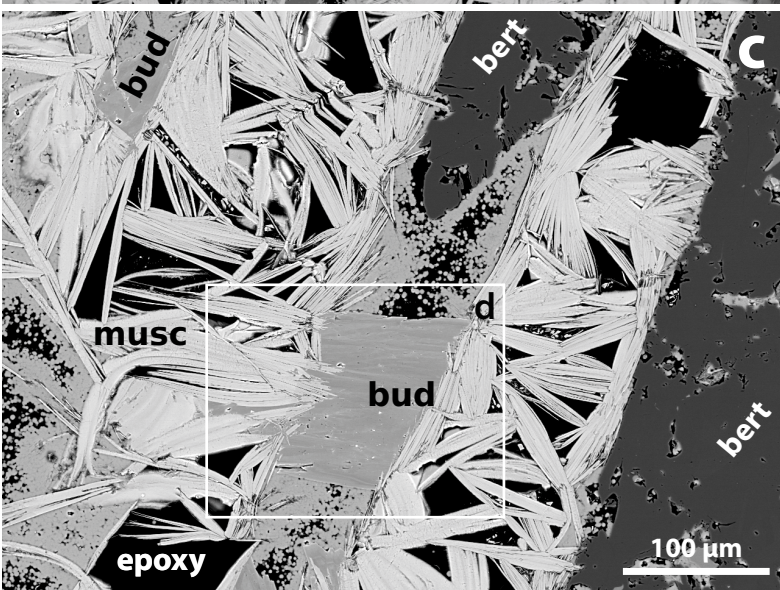
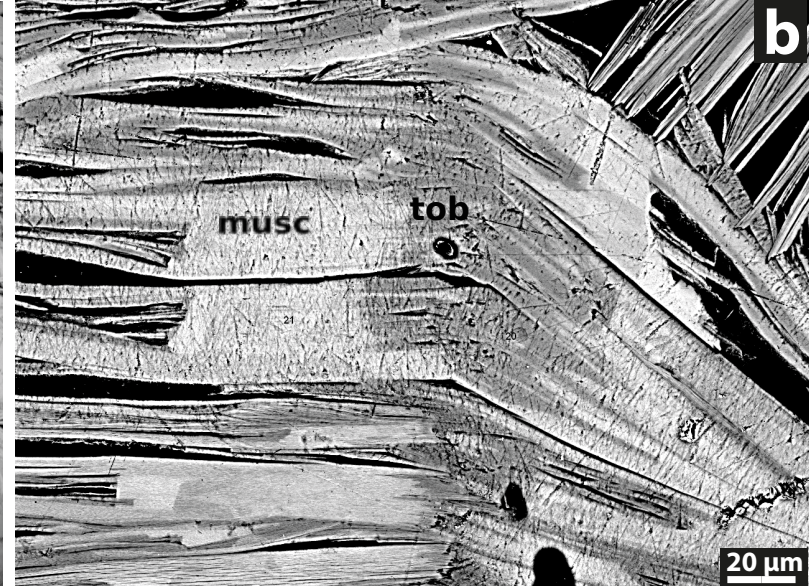
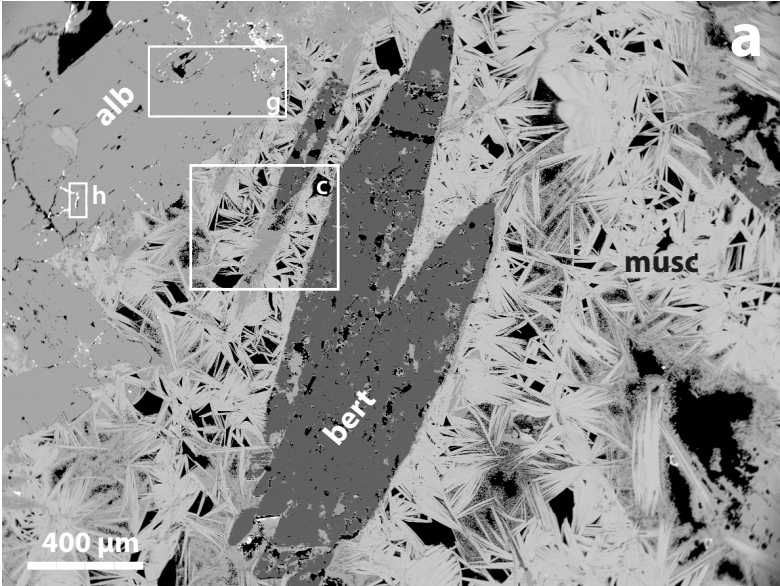


Fig. 2

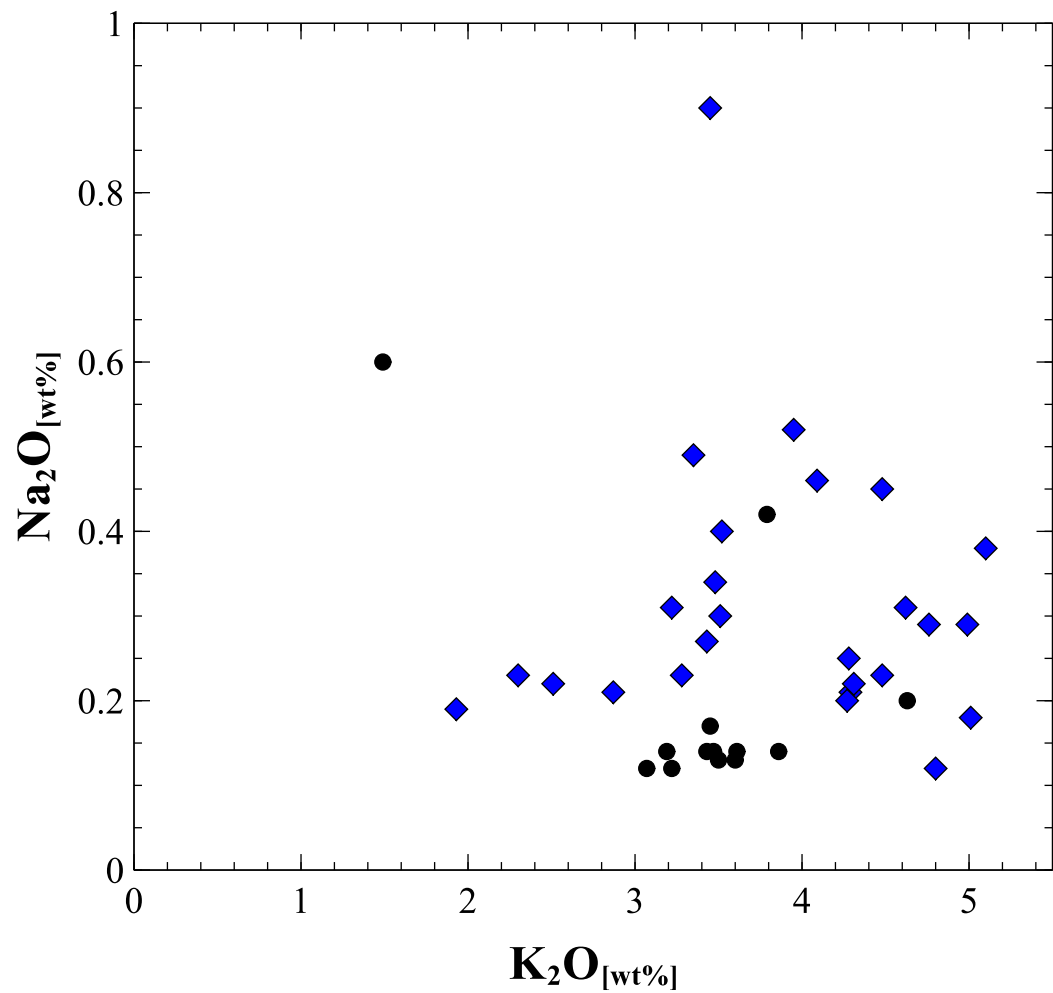
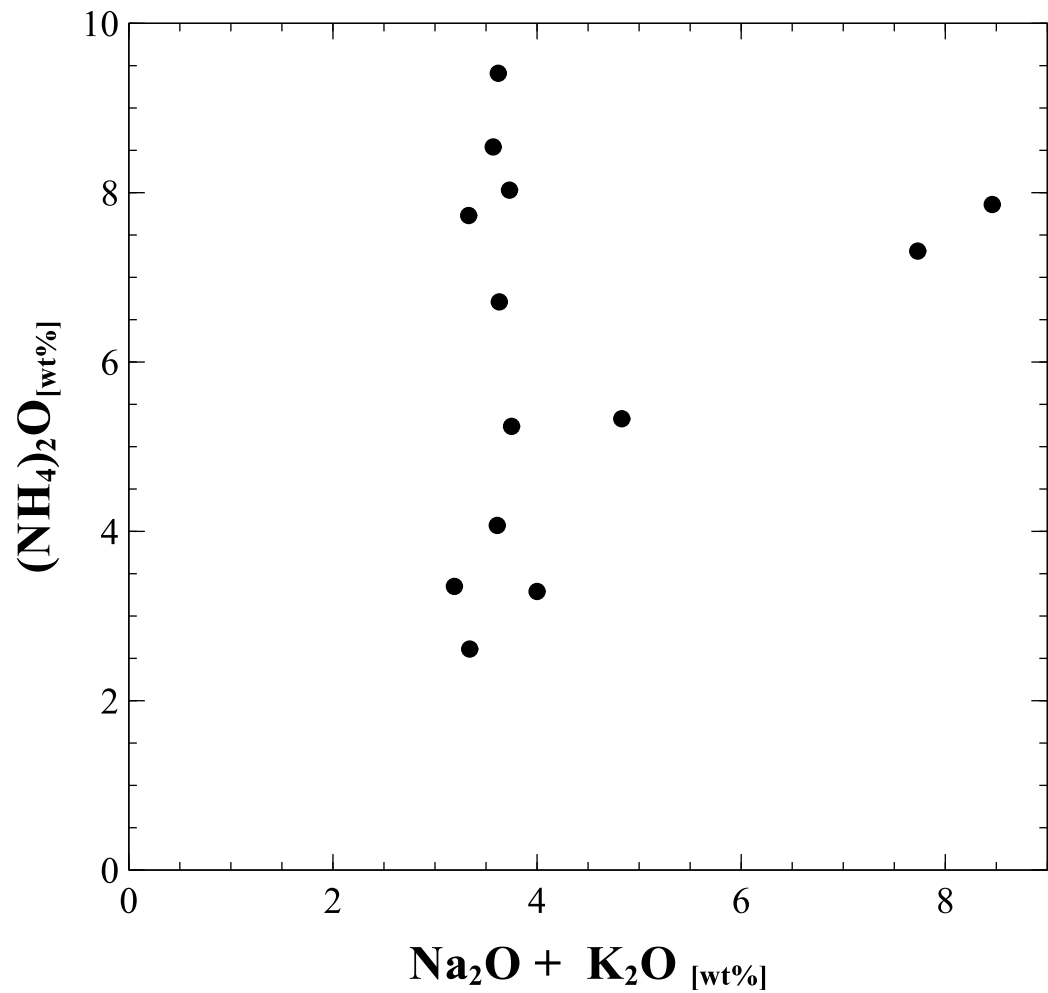


Fig. 3

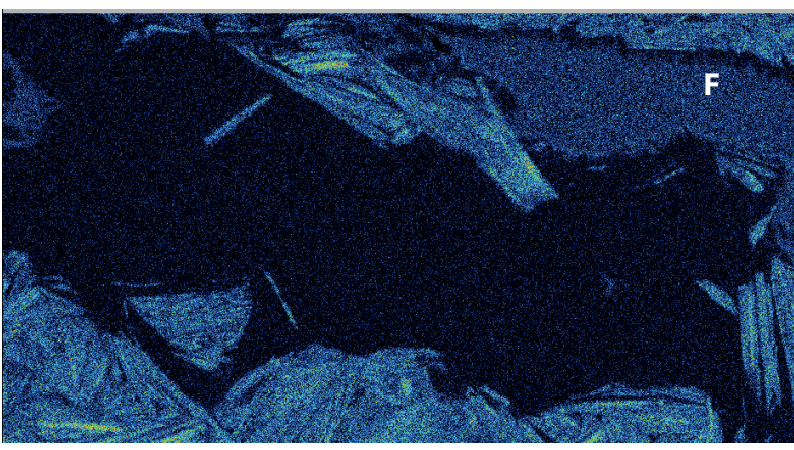
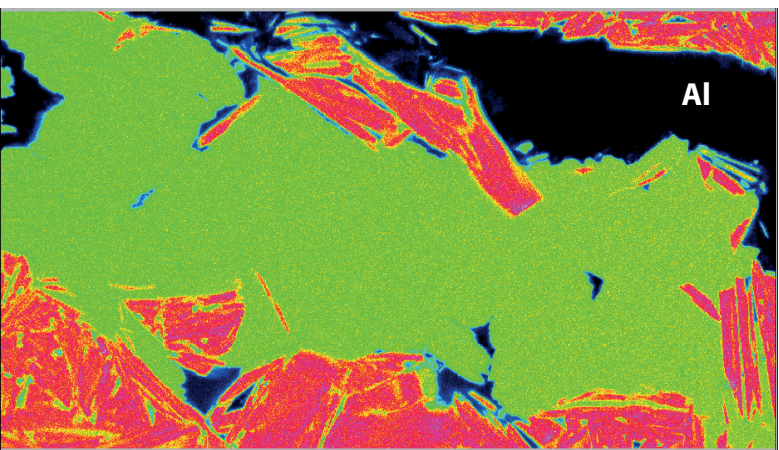
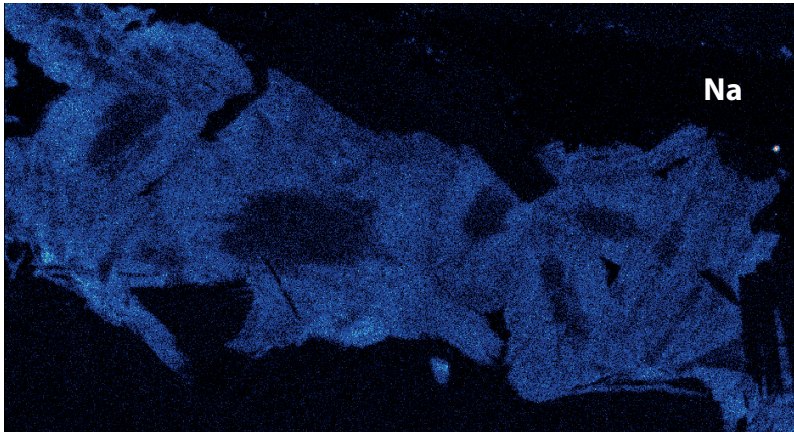
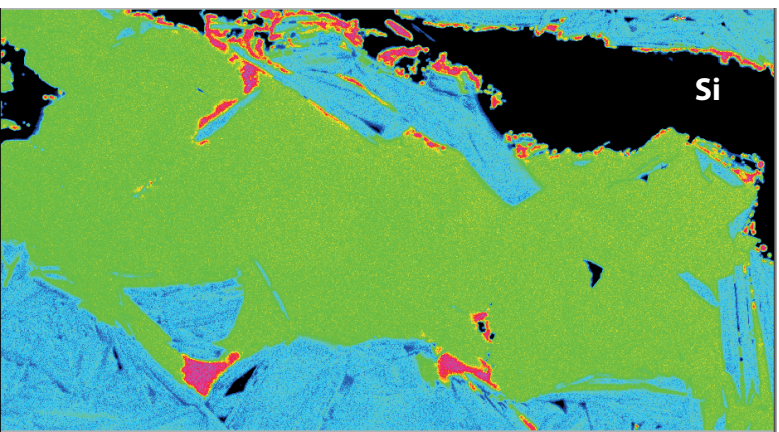
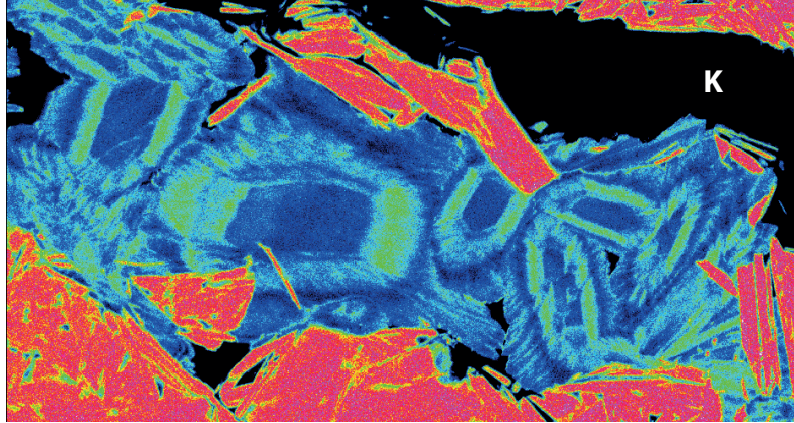
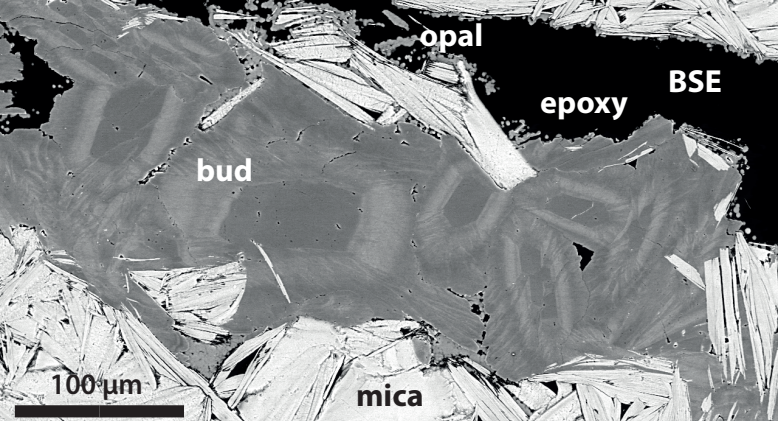


Fig. 4

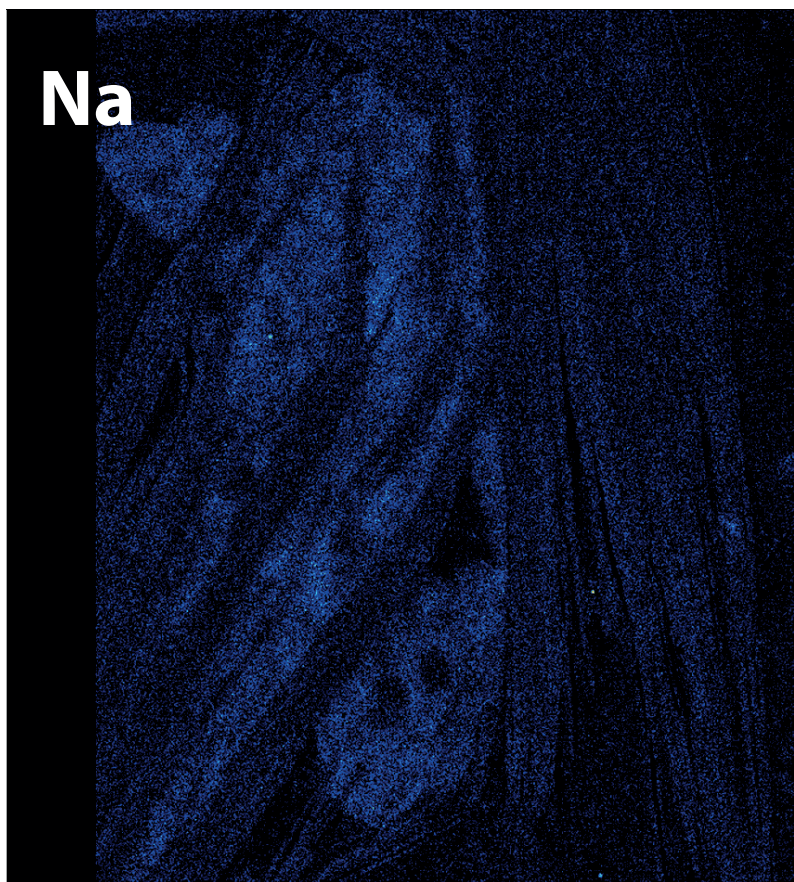
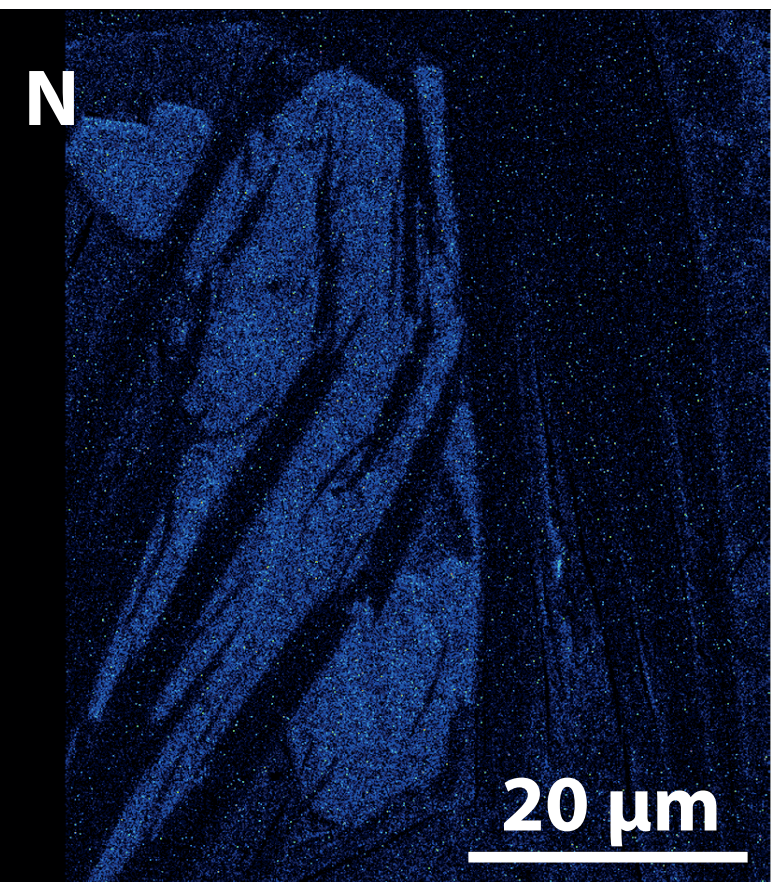
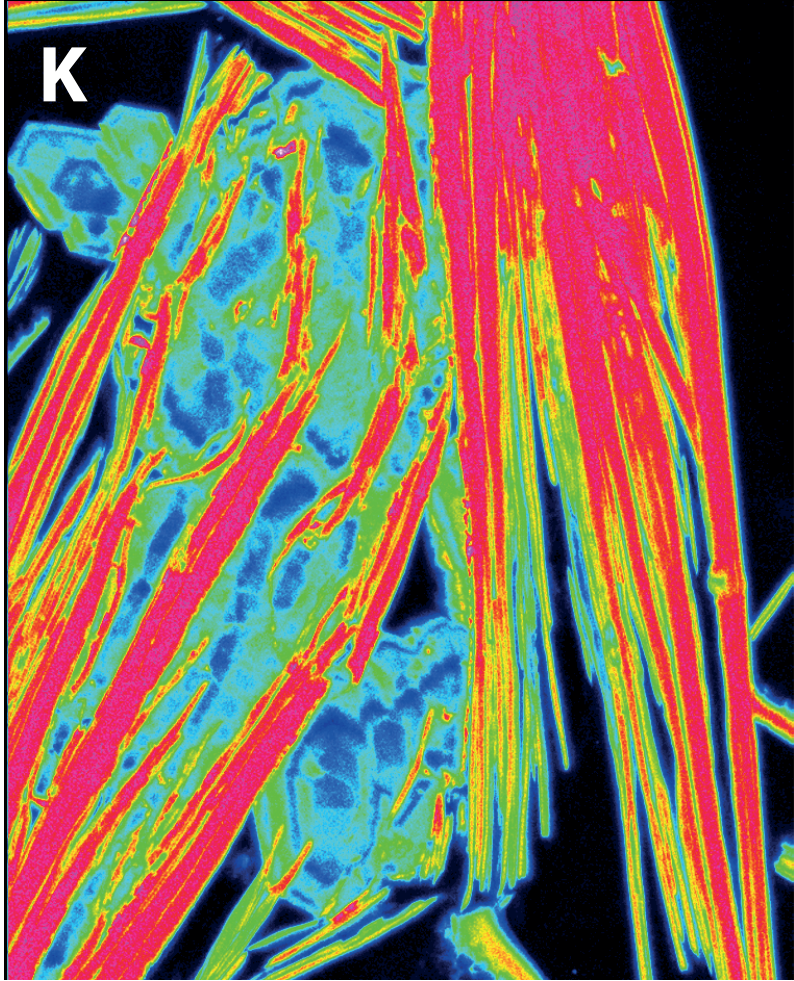


Fig. 5

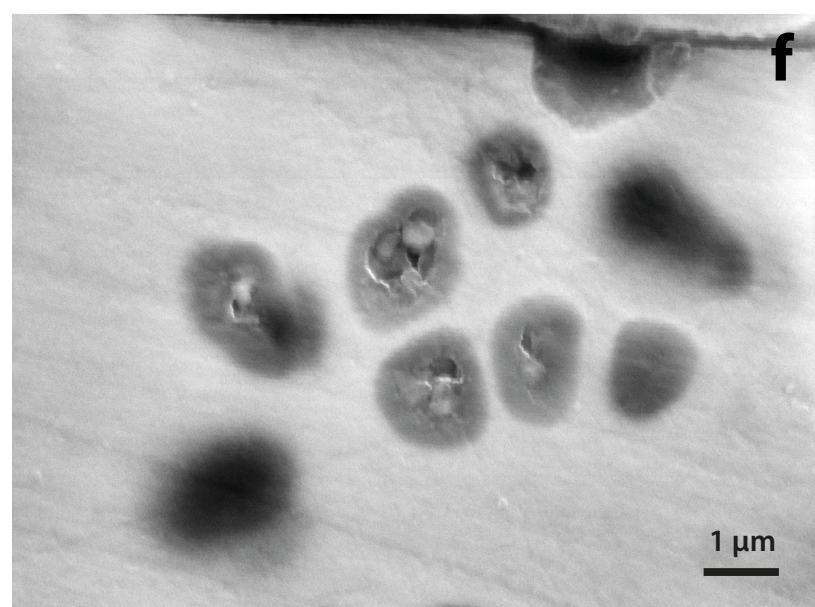
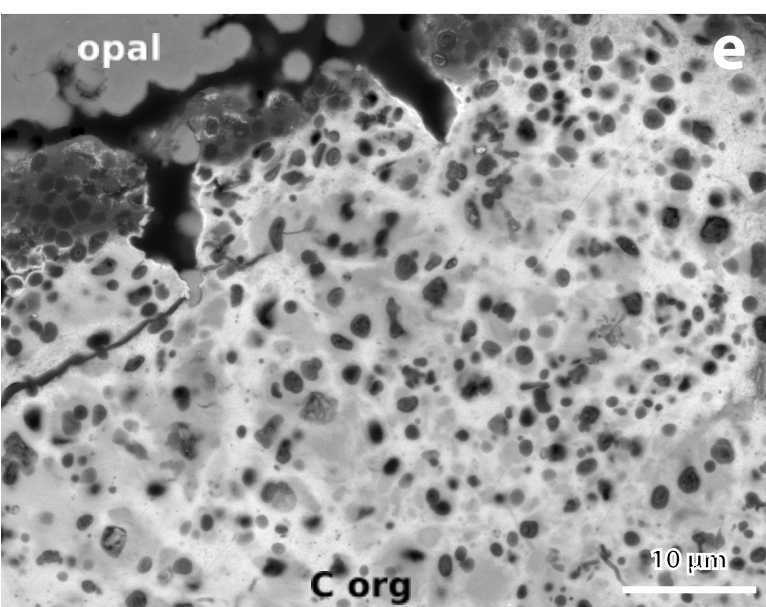
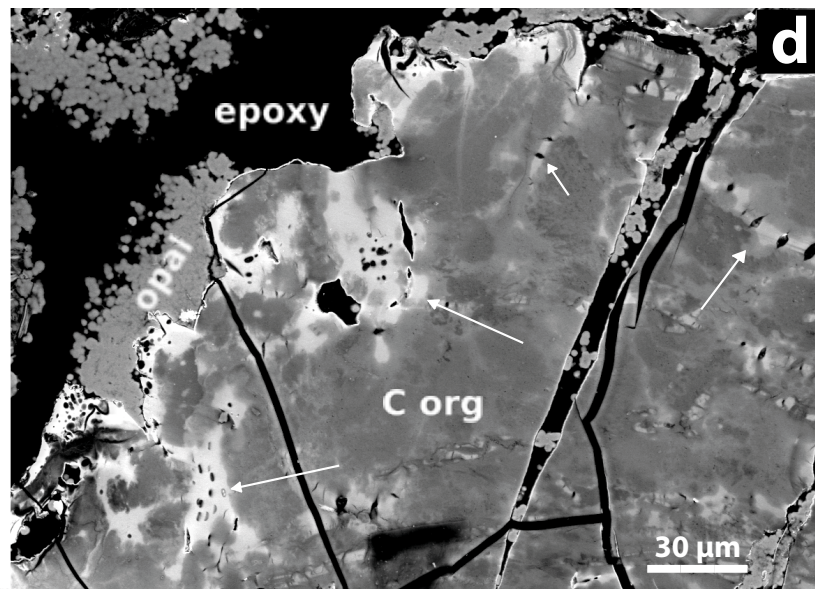
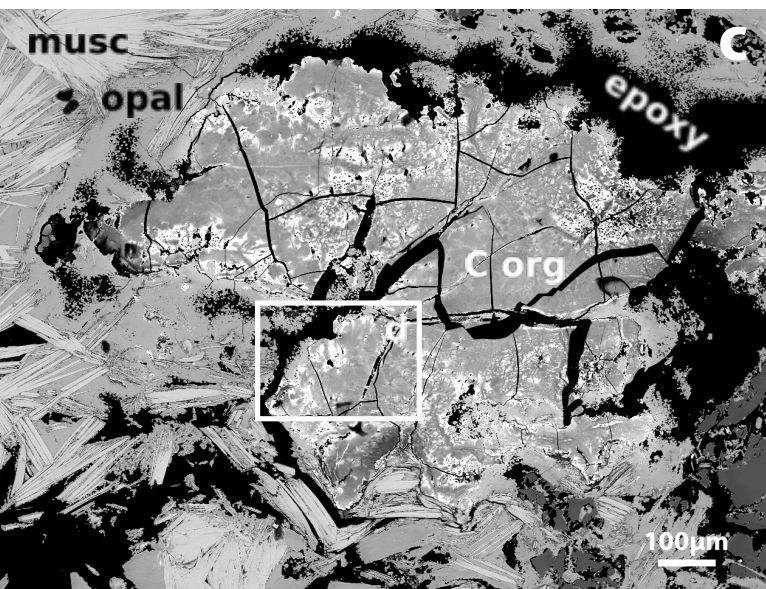
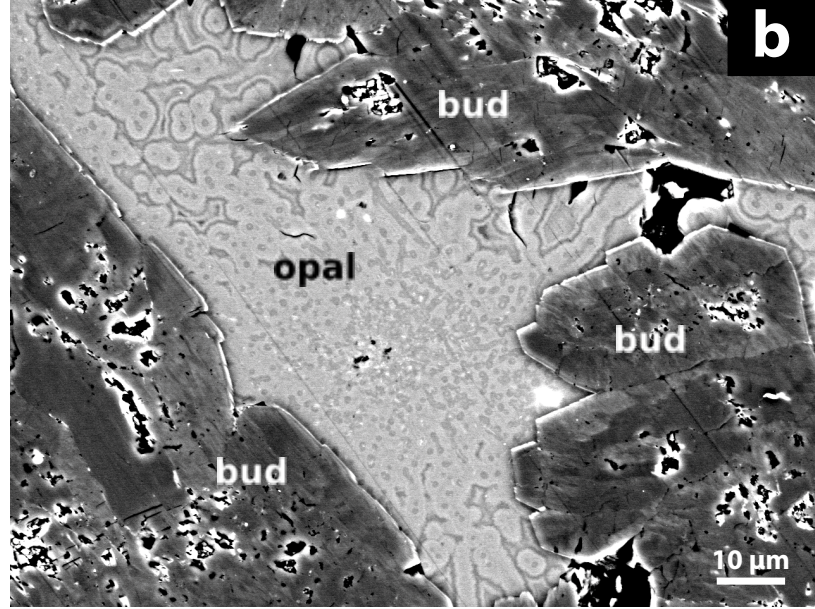
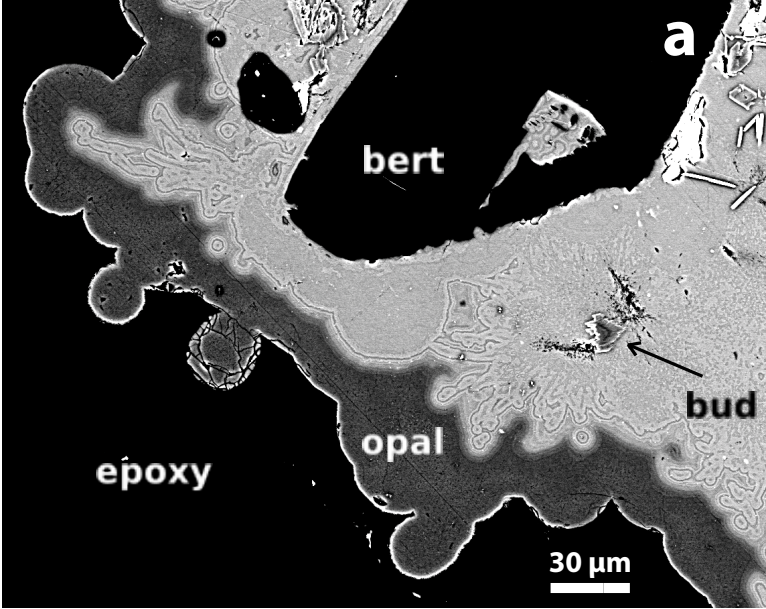


Fig. 6

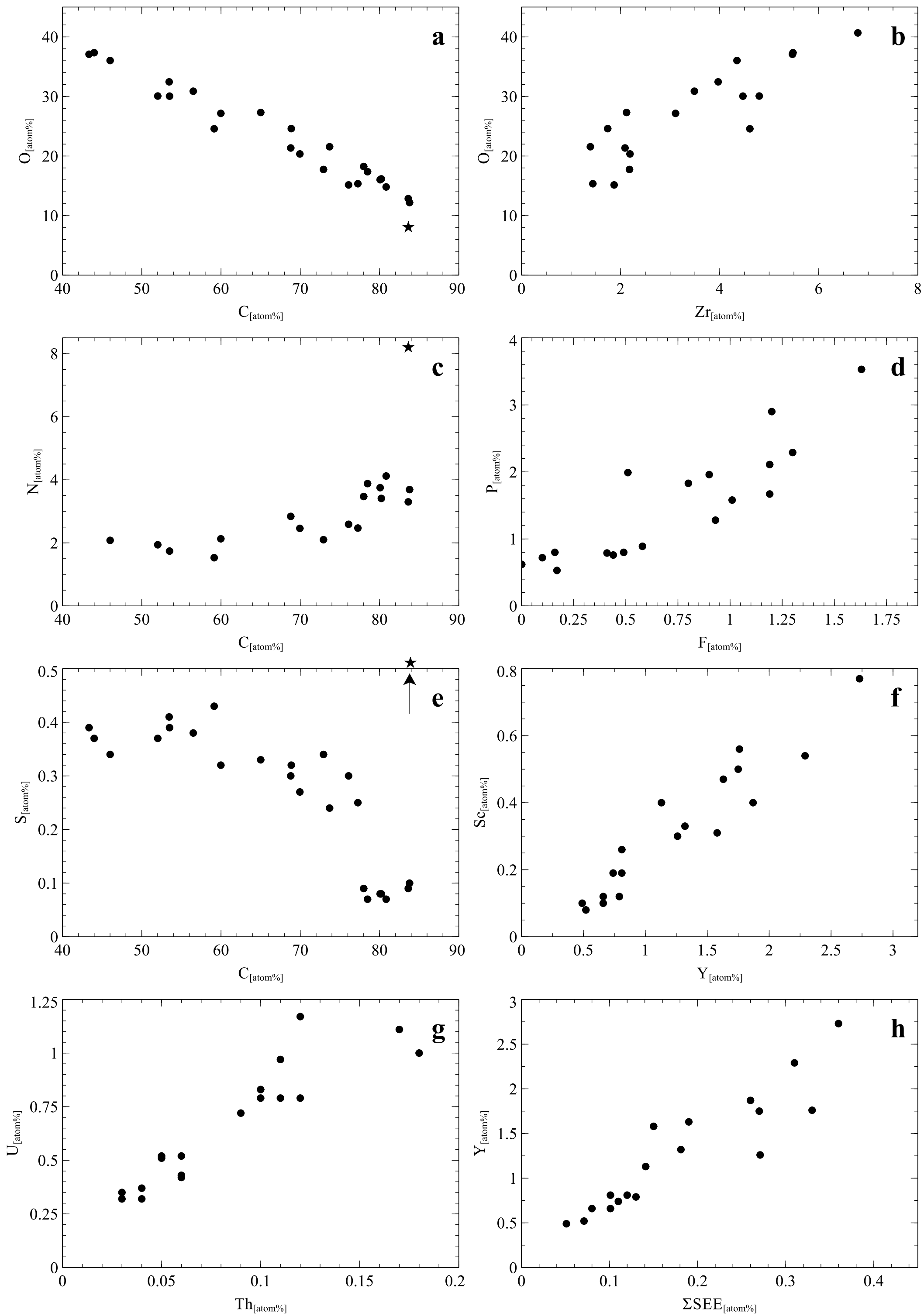


Fig. 7

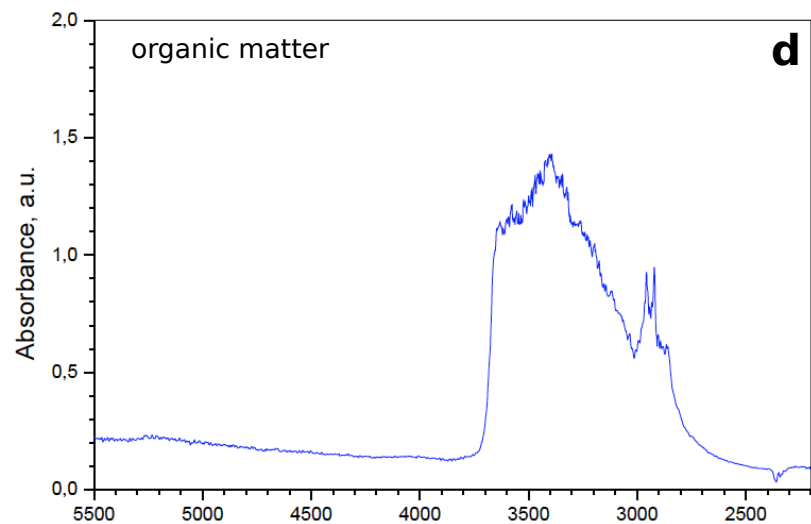
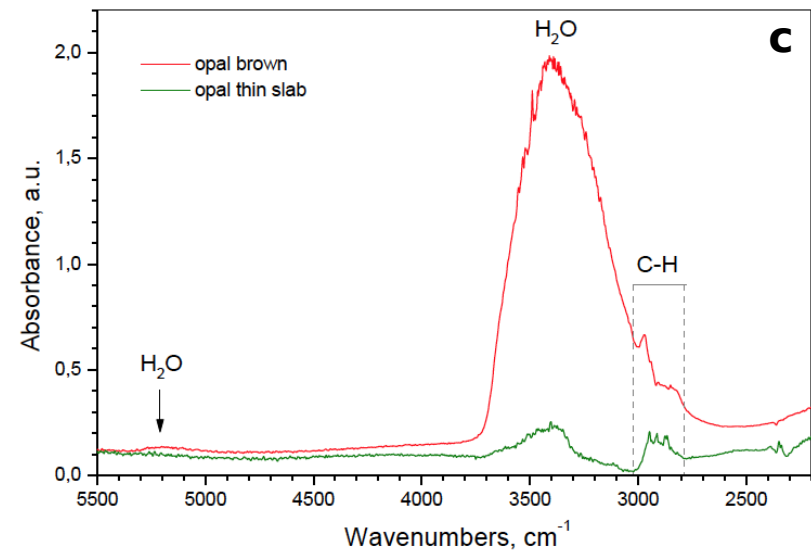
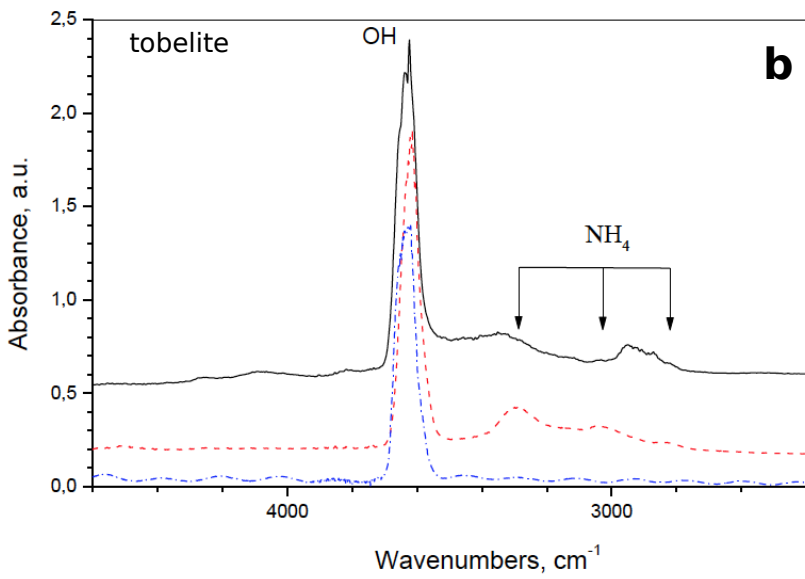
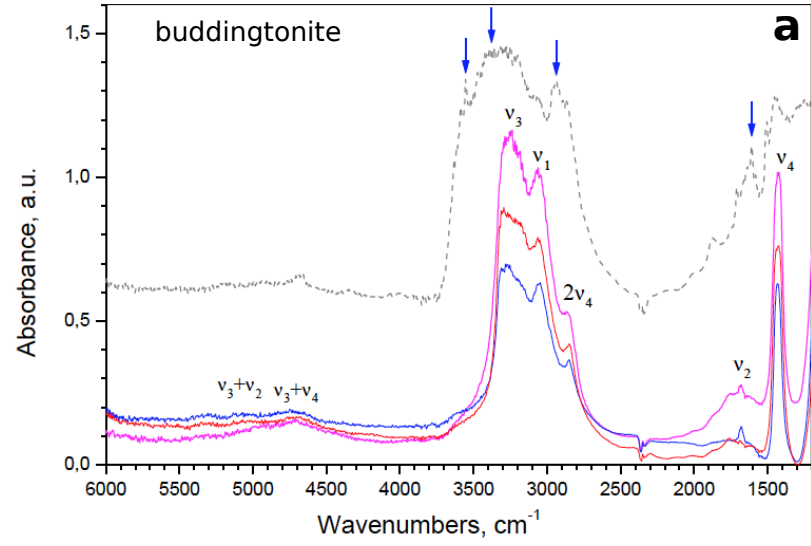


Fig. 8

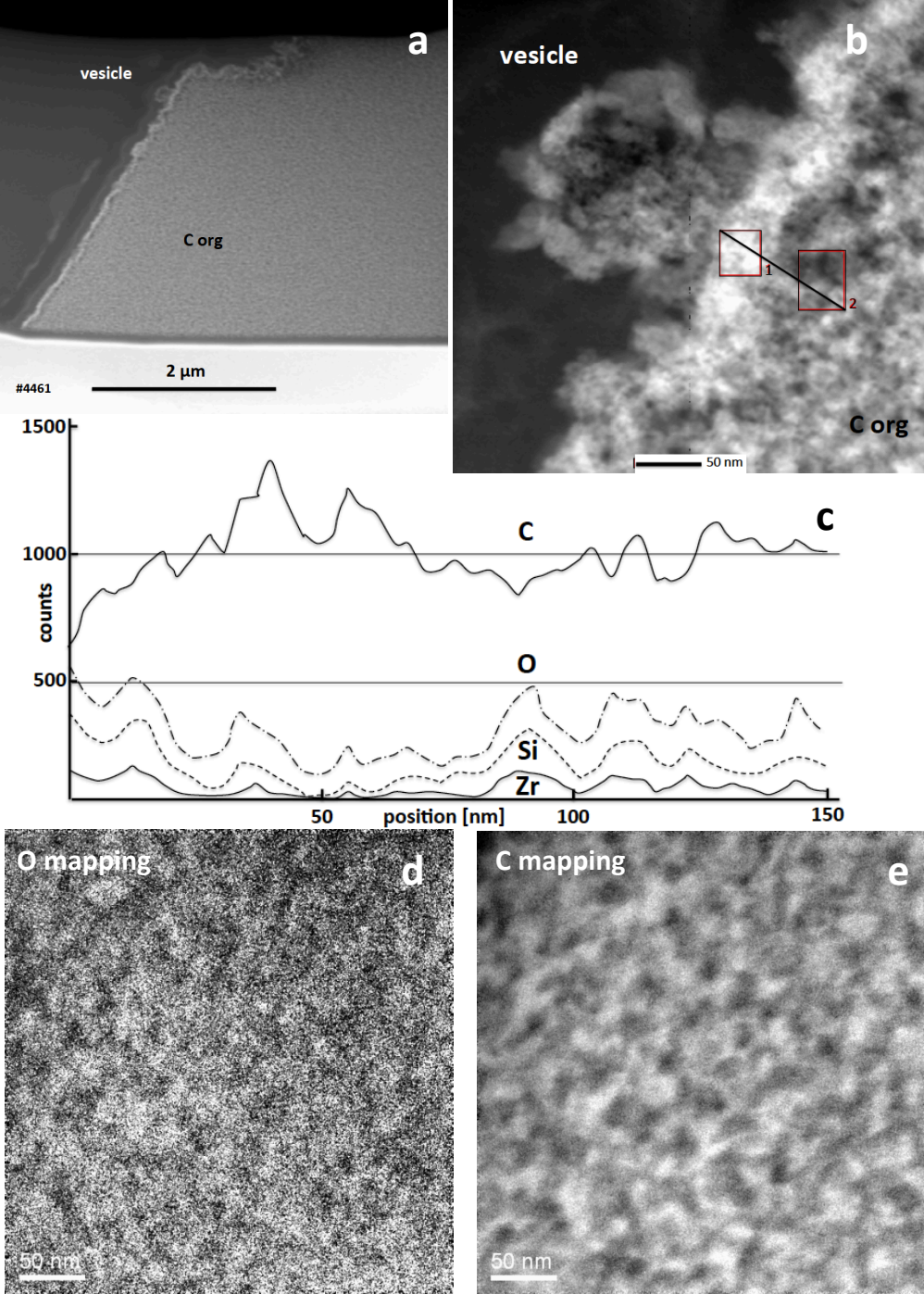


Fig. 9

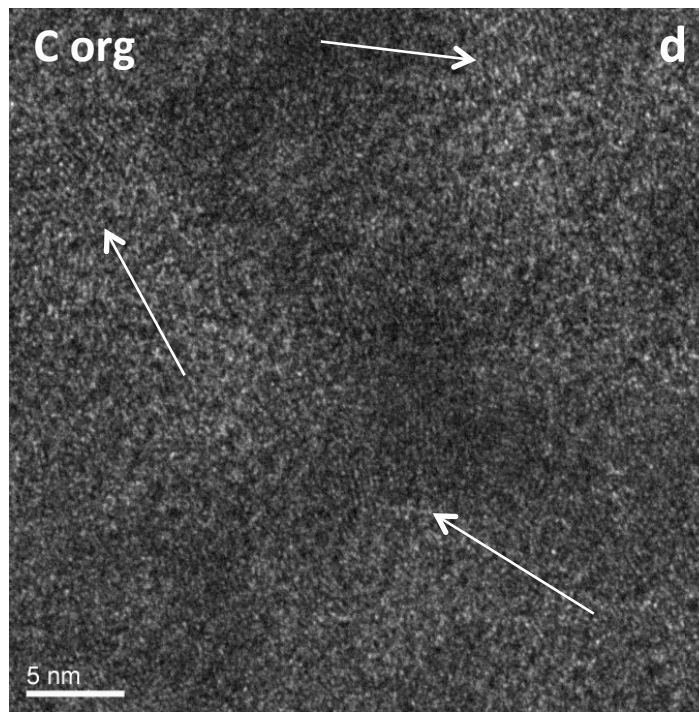
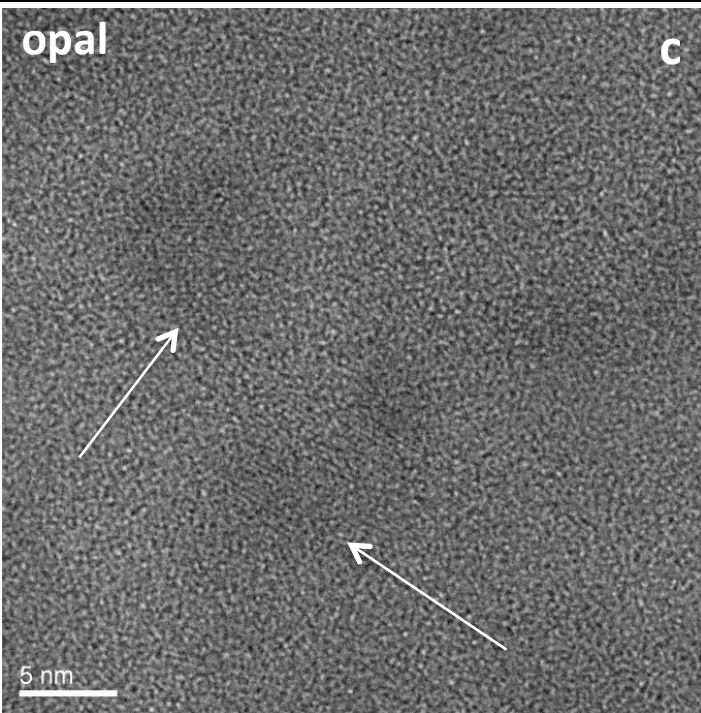
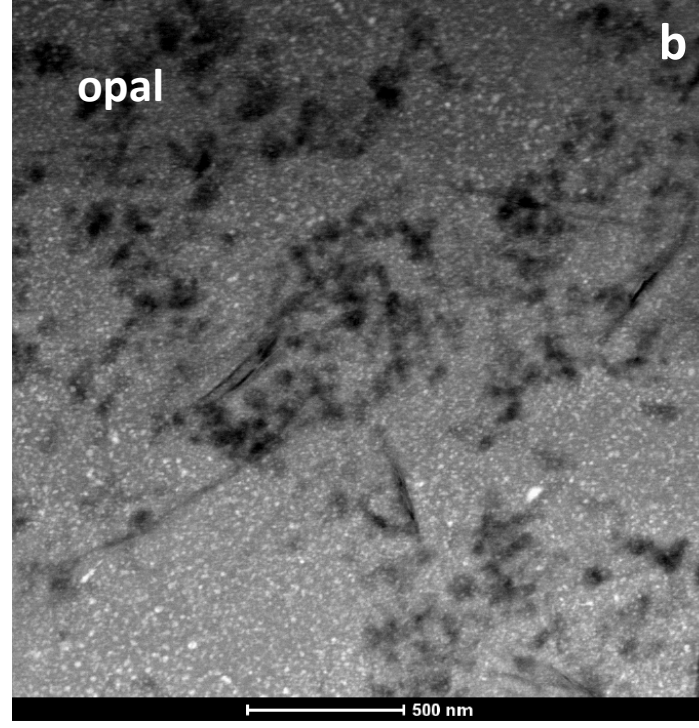
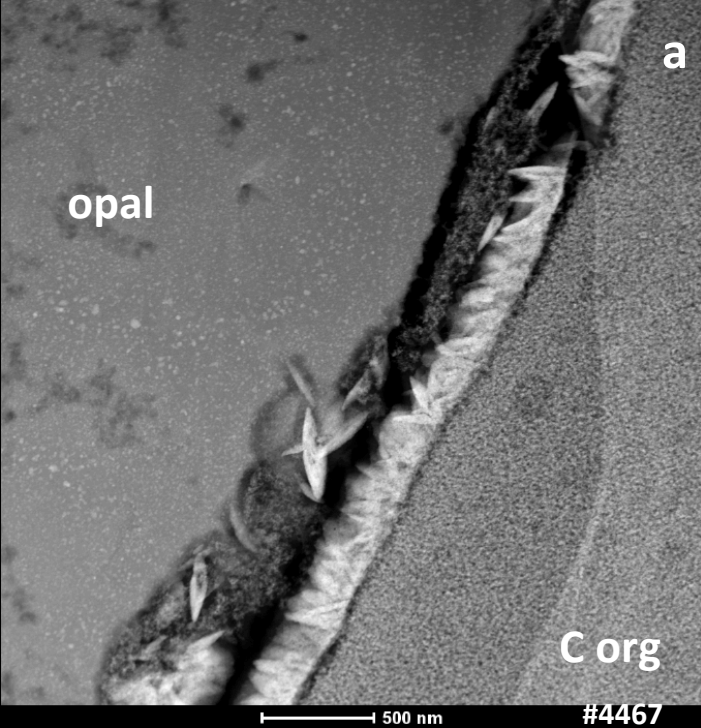


Fig. 10

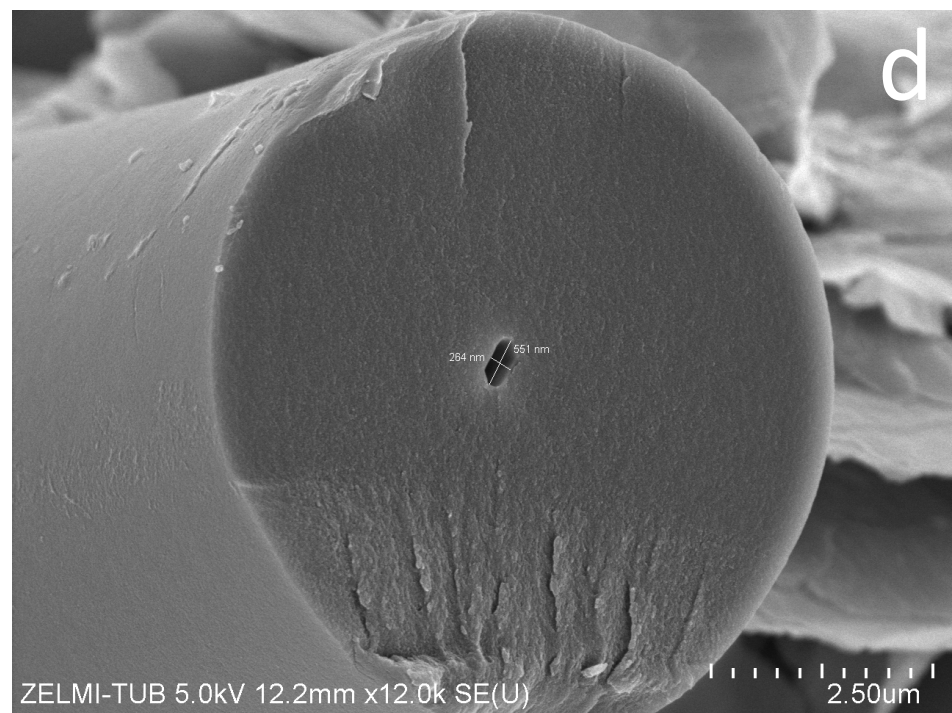
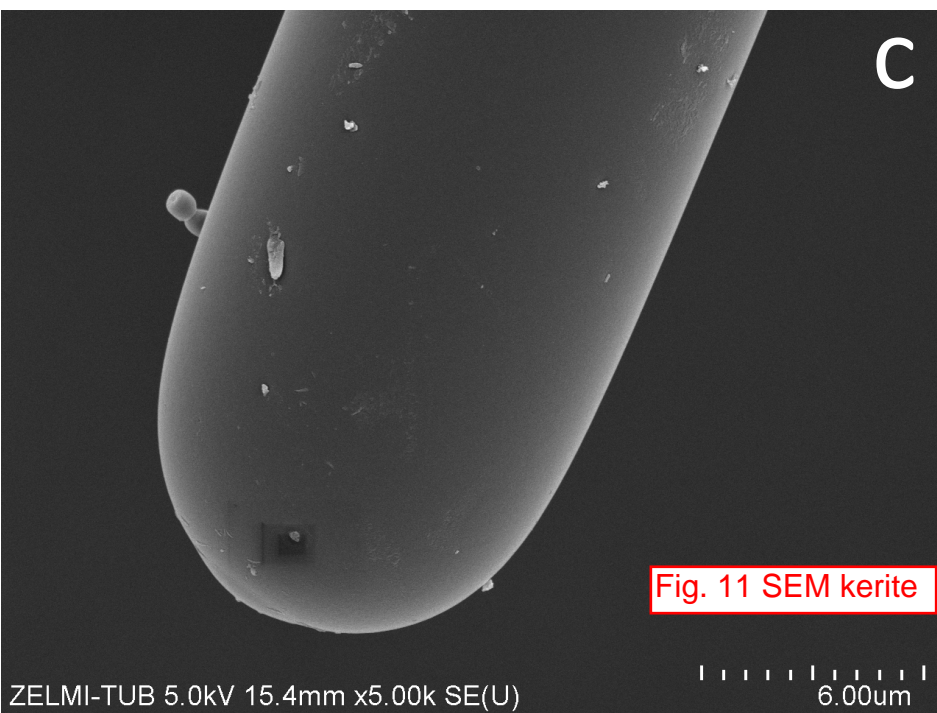
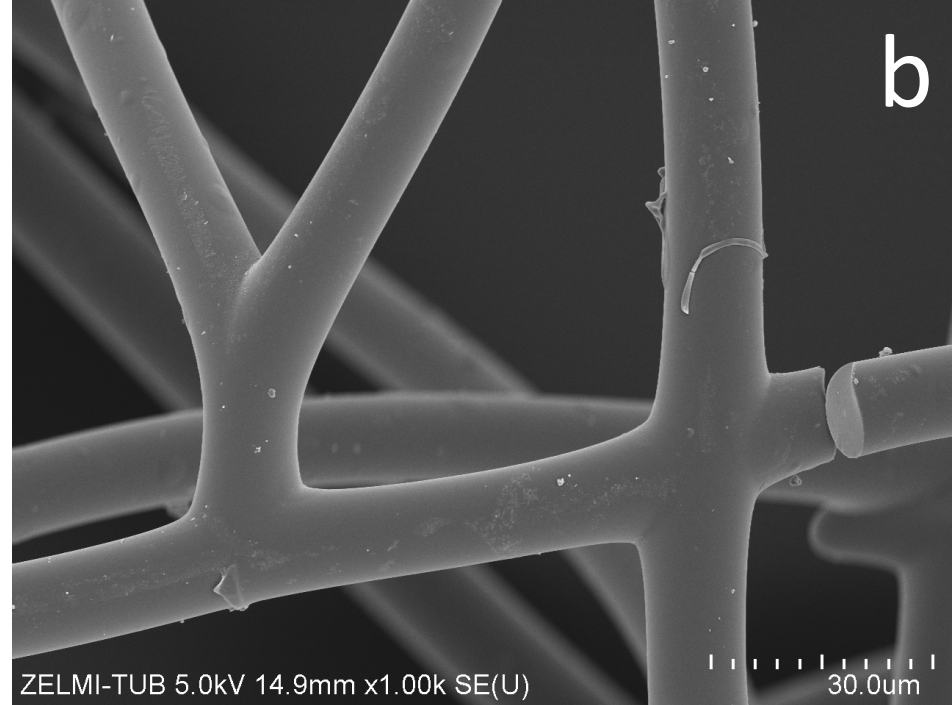
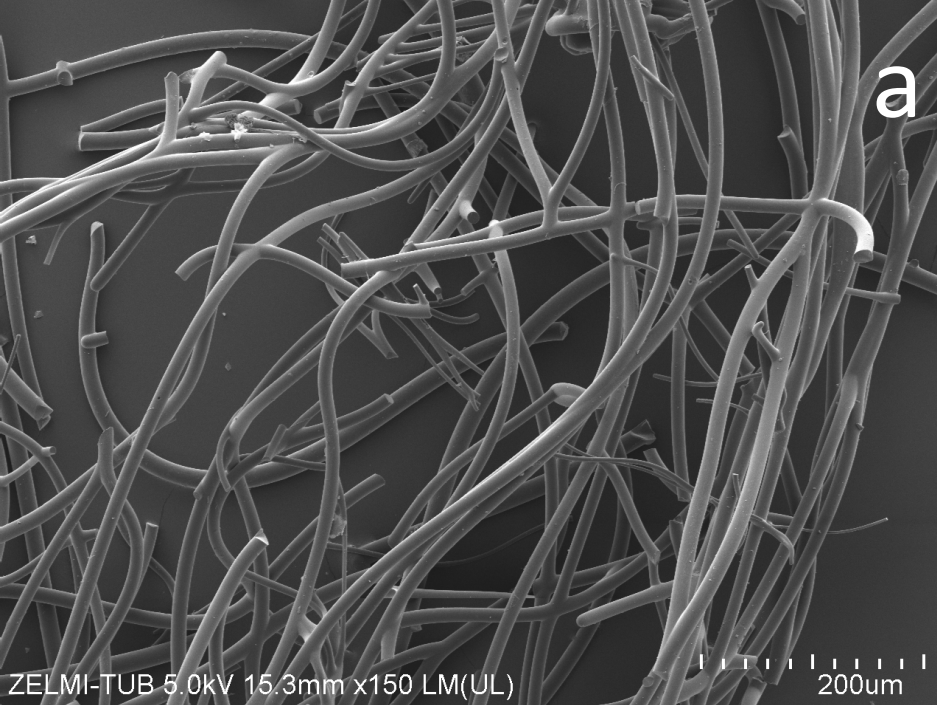


Fig. 11 SEM kerite

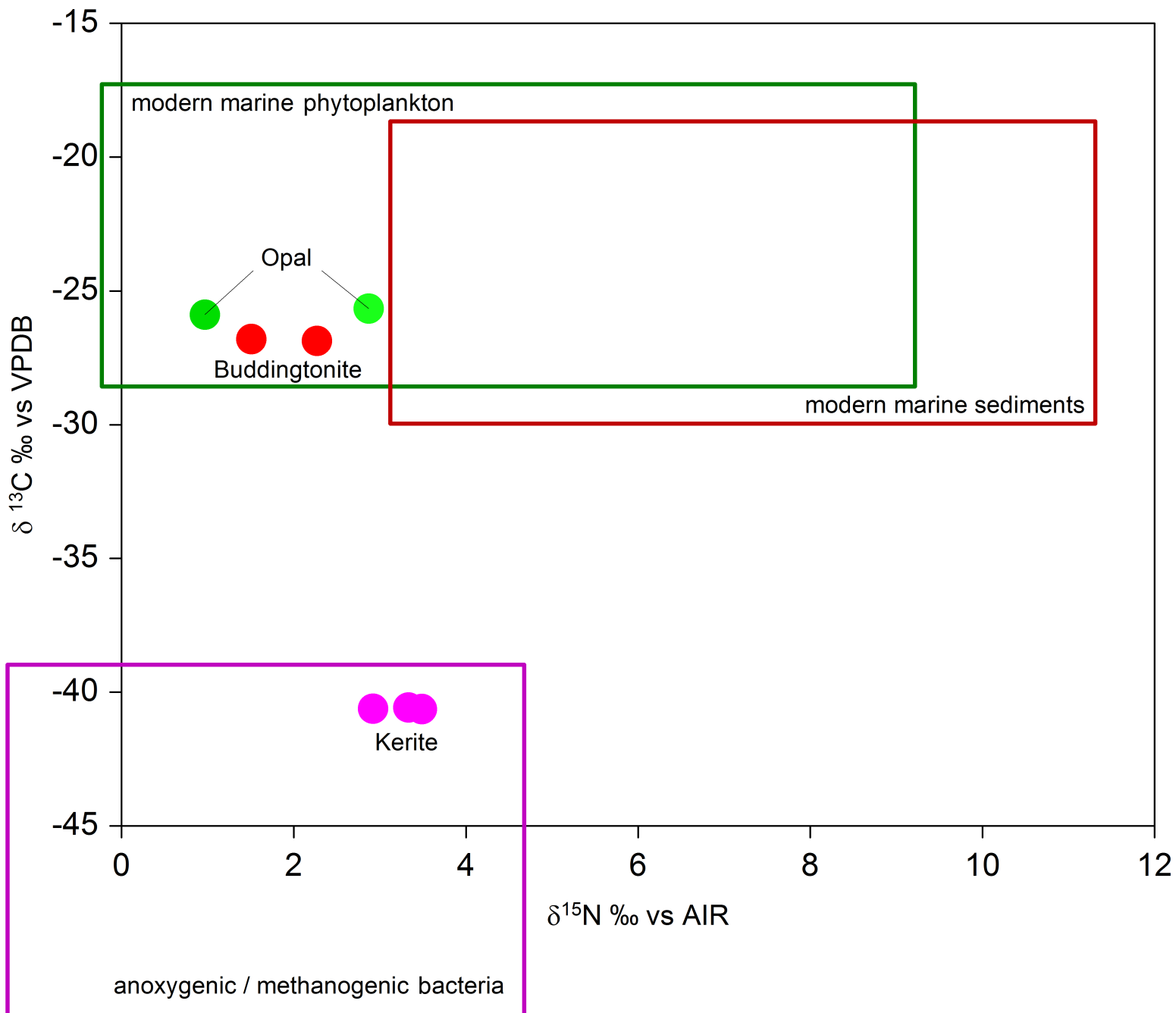


Fig. 12 C-N isotopes

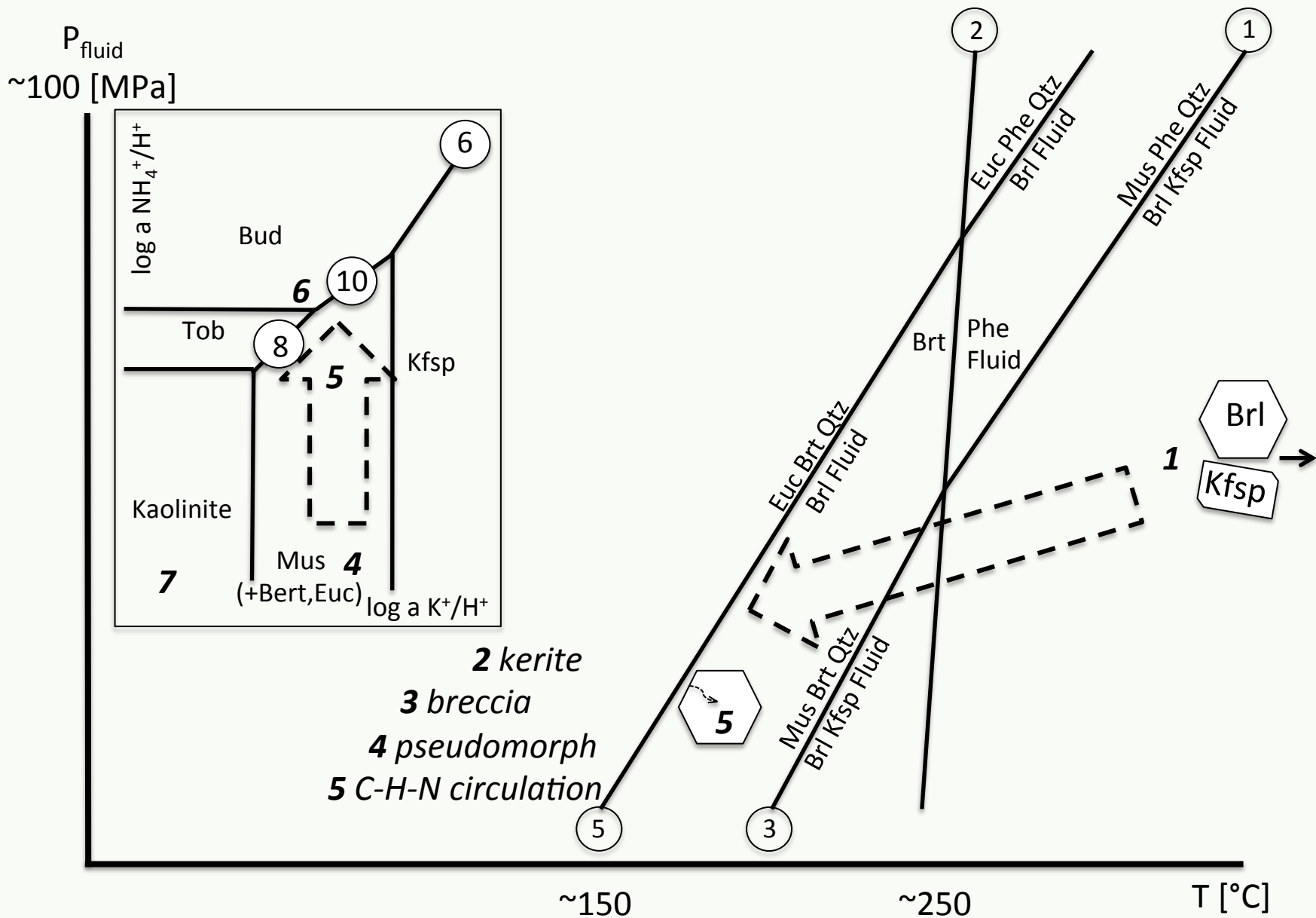


Fig. 11